



1

2 **Improvement from the satellite-derived NO<sub>x</sub> emissions on**  
3 **air quality modeling and its effect on ozone and secondary**  
4 **inorganic aerosol formation in Yangtze River Delta, China**

5

6 Yang Yang<sup>1</sup>, Yu Zhao<sup>1,2\*</sup>, Lei Zhang<sup>1</sup>, Jie Zhang<sup>3</sup>, Xin Huang<sup>4</sup>, Xuefen Zhao<sup>1</sup>,  
7 Yan Zhang<sup>1</sup>, Mengxiao Xi<sup>1</sup> and Yi Lu<sup>1</sup>

8

9 1. State Key Laboratory of Pollution Control & Resource Reuse and School of the  
10 Environment, Nanjing University, 163 Xianlin Ave., Nanjing, Jiangsu 210023, China

11 2. Jiangsu Collaborative Innovation Center of Atmospheric Environment and  
12 Equipment Technology (CICAET), Nanjing University of Information Science &  
13 Technology, Jiangsu 210044, China

14 3. Jiangsu Provincial Academy of Environmental Science, 176 North Jiangdong Rd.,  
15 Nanjing, Jiangsu 210036, China

16 4. School of the Atmospheric Sciences, Nanjing University, 163 Xianlin Ave.,  
17 Nanjing, Jiangsu 210023, China

18

19

20 \*Corresponding author: Yu Zhao

21 Phone: 86-25-89680650; email: [yuzhao@nju.edu.cn](mailto:yuzhao@nju.edu.cn)

22



23

### Abstract

24 We developed a “top-down” methodology combining the inversed chemistry  
25 transport modeling and satellite-derived tropospheric vertical column of NO<sub>2</sub>, and  
26 estimated the NO<sub>x</sub> emissions of Yangtze River Delta (YRD) region at a horizontal  
27 resolution of 9 km for January, April, July and October 2016. The effect of the  
28 top-down emission estimation on air quality modeling, and the response of ambient  
29 ozone (O<sub>3</sub>) and secondary inorganic aerosols (SO<sub>4</sub><sup>2-</sup>, NO<sub>3</sub><sup>-</sup>, and NH<sub>4</sub><sup>+</sup>, SNA) to the  
30 changed precursor emissions were evaluated with the Community Multi-scale Air  
31 Quality (CMAQ) system. The top-down estimates of NO<sub>x</sub> emissions were smaller  
32 than those in a national emission inventory, MEIC (i.e., the “bottom-up” estimates),  
33 for all the four months, and the monthly mean was calculated at 260.0 Gg/month,  
34 24% less than the bottom-up one. The NO<sub>2</sub> concentrations simulated with the  
35 bottom-up estimate of NO<sub>x</sub> emissions were clearly higher than the ground  
36 observation, indicating the possible overestimation in current emission inventory  
37 attributed to its insufficient consideration of recent emission control in the region. The  
38 model performance based on top-down estimate was much better, and the biggest  
39 change was found for July with the normalized mean bias (NMB) and normalized  
40 mean error (NME) reduced from 111% to -0.4% and from 111% to 33%, respectively.  
41 The results demonstrate the improvement of NO<sub>x</sub> emission estimation with the  
42 nonlinear inversed modeling and satellite observation constraint. With the smaller  
43 NO<sub>x</sub> emissions in the top-down estimate than the bottom-up one, the elevated  
44 concentrations of ambient O<sub>3</sub> were simulated for most YRD and they were closer to  
45 observation except for July, implying the VOC (volatile organic compound)-limit  
46 regime of O<sub>3</sub> formation. With available ground observations of SNA in the YRD,  
47 moreover, better model performance of NO<sub>3</sub><sup>-</sup> and NH<sub>4</sub><sup>+</sup> were achieved for most  
48 seasons, implying the effectiveness of precursor emission estimation on the  
49 simulation of secondary inorganic aerosols. Through the sensitivity analysis of O<sub>3</sub>  
50 formation for April 2016, the decreased O<sub>3</sub> concentrations were found for most YRD  
51 region when only VOCs emissions were reduced or the reduced rate of VOCs



52 emissions was two times of that of  $\text{NO}_x$ , implying the crucial role of VOCs control on  
53  $\text{O}_3$  pollution abatement. The SNA level for January 2016 was simulated to decline  
54 12% when 30% of  $\text{NH}_3$  emissions were reduced, while the change was much smaller  
55 with the same reduced rate for  $\text{SO}_2$  or  $\text{NO}_x$ . The result suggests that reducing  $\text{NH}_3$   
56 emissions was the most effective way to alleviate SNA pollution for YRD in winter.

57

## 58 **1. Introduction**

59 Nitrogen oxides ( $\text{NO}_x = \text{NO}_2 + \text{NO}$ ) play an important role on the formation of  
60 ambient ozone ( $\text{O}_3$ ) and secondary inorganic aerosol (SIA). The  $\text{NO}_x$  emission  
61 inventories are necessary input of the air quality model (AQM), and have a great  
62 influence on the simulation particularly for  $\text{NO}_2$ ,  $\text{O}_3$  and SIA (Zhou et al., 2017; Chen  
63 et al., 2019a). Moreover, it is crucial for exploring the sources of atmospheric  
64 pollution of  $\text{O}_3$  and fine particles (particles with aerodynamic diameter smaller than  
65  $2.5\ \mu\text{m}$ ,  $\text{PM}_{2.5}$ ) with AQM.

66 The  $\text{NO}_x$  emission inventories were usually developed with a bottom-up method,  
67 in which the emissions were calculated based on the activity data (e.g., fuel  
68 consumption and industrial production) and emission factors (the emissions per unit  
69 of activity data) by source category and region. Bias existed commonly in the  
70 bottom-up inventories, due mainly to the uncertainty of economic and energy  
71 statistics and fast changes in the emission control measures, especially in developing  
72 countries like China (Granier et al., 2011; Saikawa et al., 2017; Zhang et al., 2019). To  
73 improve the emission estimation, an inversed “top-down” method has been developed  
74 based on satellite observation and AQM (Martin et al., 2003; Zhao and Wang et al.,  
75 2009; Zyrichidou et al., 2015; Yang et al., 2019a). The emissions were corrected  
76 based on the difference between the modeled and observed tropospheric vertical  
77 column densities (TVCDs) of  $\text{NO}_2$ , and the response coefficient of  $\text{NO}_2$  TVCDs to  
78 emissions ((Martin et al., 2003; Cooper et al., 2017). With higher temporal and spatial  
79 resolution than other instruments, the  $\text{NO}_2$  TVCDs from Ozone Monitoring  
80 Instrument (OMI) were frequently used (Kurokawa et al., 2009; Gu et al., 2014; de



81 Foy et al., 2015; Kong et al., 2019; Yang et al., 2019a).  
82 Currently, the top-down methods were mainly developed at the global or national  
83 scale with relatively coarse horizontal resolution (Martin et al., 2003; Miyazaki et al.,  
84 2012; Jena et al., 2014). For example, Martin et al. (2003) and Miyazaki et al. (2012)  
85 estimated the global top-down NO<sub>x</sub> emissions at the horizontal resolution of 2° × 2.5°  
86 and 2.8° × 2.8°, respectively. As reported by Martin et al. (2003), the satellite-derived  
87 NO<sub>x</sub> emissions for 1996-1997 were higher than bottom-up ones by 50-100% in the Po  
88 Valley, Tehran, and Riyadh urban areas. Miyazaki et al. (2012) suggested that the  
89 NO<sub>x</sub> emissions were underestimated with the bottom-up method over eastern China,  
90 eastern United States, southern Africa, and central-western Europe. In India, the  
91 top-down estimation of annual NO<sub>x</sub> emission at the horizontal resolution of 0.5° ×  
92 0.5° was 7-60% smaller than various bottom-up ones in 2005 (Jena et al., 2014). With  
93 the TVCDs from OMI and another instrument (Global Ozone Monitoring Experiment,  
94 GOME), the difference in NO<sub>x</sub> emission estimation for China was quantified at 0.4  
95 Tg N/yr at the resolution of 70 × 70 km (Gu et al., 2014). The estimates were limited at  
96 the regional scale with finer resolution. In China, great differences exist in the levels  
97 and patterns of air pollution across the regions, attributed partly to a big variety of air  
98 pollutant sources across the country. To achieve the target of air quality improvement  
99 required by the central government, varied air pollution control plans were usually  
100 developed and implemented at the city/provincial levels. Therefore, the top-down  
101 estimates in NO<sub>x</sub> emissions at finer horizontal resolution are in great need for  
102 understanding the primary sources of NO<sub>2</sub> pollution and demonstrating the effect of  
103 emission control at the regional scale.

104 Biases existed in the top-down estimates resulting from the uncertainties of the  
105 inversed method and satellite observation (Cooper et al., 2017; Ding et al., 2017; Liu  
106 et al., 2019; Yang et al., 2019a; b), and they could further influence the reliability of  
107 AQM and the rationality of control measures. At present, those estimates of NO<sub>x</sub>  
108 emissions were usually evaluated with satellite observation. For example, the bias  
109 between the NO<sub>2</sub> TVCDs from OMI observation and AQM based on the top-down  
110 NO<sub>x</sub> emission estimation was  $-30.8 \pm 69.6 \times 10^{13}$  molecules cm<sup>-2</sup> in winter in India



111 (Jena et al., 2014). The linear correlation coefficient ( $R^2$ ) between OMI and AQM  
112 with the top-down emission estimates could reach 0.84 in Europe (Visser et al., 2019).  
113 Compared to the satellite observation with relatively large uncertainty (Yang et al.,  
114 2019b; Liu et al., 2019), surface concentrations that better represent the effect of air  
115 pollution on human health and the ecosystems were less applied in the evaluation of  
116 the top-down estimates of  $\text{NO}_x$  emissions. Limited studies were conducted at coarse  
117 horizontal resolutions at the national scale. For example, Liu et al. (2018) found that  
118 the normalized mean error (NME) between the observed and simulated  $\text{NO}_2$   
119 concentrations based on the top-down estimate of  $\text{NO}_x$  emissions could reach 32% in  
120 China at the resolution of  $0.25^\circ \times 0.25^\circ$ . Besides  $\text{NO}_2$ , the estimation of  $\text{NO}_x$   
121 emissions also play an important and complicated role on simulation of secondary air  
122 pollutant concentrations including  $\text{O}_3$  and SIA, and the response of secondary  
123 pollution to the primary emissions was commonly nonlinear. For example, Wang et al.  
124 (2019) found that the simulated  $\text{O}_3$  concentrations in Shanghai (the most developed  
125 city in eastern China) could increase over 20% with a 60% reduction in  $\text{NO}_x$   
126 emissions in summer 2016, implying a clear “VOC-limit” pattern for the  $\text{O}_3$  formation  
127 in the mega city. For the response of SIA to  $\text{NO}_x$  emissions, the  $\text{NH}_4^+$  and  $\text{SO}_4^{2-}$   
128 concentrations at an urban site in another mega city Nanjing in eastern China were  
129 simulated to increase 1.9% and 2.8% with a 40% abatement of  $\text{NO}_x$  emissions in  
130 autumn 2014, respectively, due to the weakened competition of SIA formation against  
131  $\text{SO}_2$  (Zhao et al., 2020). To our knowledge, however, the relatively new information  
132 from the inversed modeling of  $\text{NO}_x$  emissions has not been sufficiently incorporated  
133 into the SIA and  $\text{O}_3$  analyses with AQM in China.

134 Located in eastern China, the Yangtze River Delta (YRD) region including the  
135 city of Shanghai and the provinces of Anhui, Jiangsu and Zhejiang is one of the most  
136 developed and heavy-polluted regions in the country. The air quality for most cities in  
137 YRD failed to meet National Ambient Air Quality Standard (NAAQS) Class II in  
138 2016 (MEPPRC, 2017).  $\text{NO}_x$  emissions made great contributions to the severe air  
139 pollution in the region. Based on an offline-sampling and measurement study, for  
140 example, the annual average of the  $\text{NO}_3^-$  mass fraction to the total  $\text{PM}_{2.5}$  reached 19%



141 in Shanghai in 2014, and it was significantly elevated in the pollution event periods  
142 (Ming et al., 2017). In this study, we chose the YRD to estimate the NO<sub>x</sub> emissions  
143 with the inversed method and to explore their influence on the air quality modeling.  
144 The top-down estimates in NO<sub>x</sub> emissions were firstly obtained with the nonlinear  
145 inversed method and OMI-derived NO<sub>2</sub> TVCDs for 2016. The advantage of the  
146 top-down estimation against on the bottom-up one was then evaluated with the AQM  
147 and abundant ground-based NO<sub>2</sub> concentrations. The influences of the top-down  
148 estimation in NO<sub>x</sub> emissions were further detected on O<sub>3</sub> and SIA modeling.  
149 Sensitivity analyses were conducted by changing the emissions of precursors to  
150 investigate the sources and potential control approaches of O<sub>3</sub> and SIA pollutions for  
151 the region.

## 152 2. Data and Methods

### 153 2.1 The top-down estimation of NO<sub>x</sub> emissions

154 The top-down estimation of NO<sub>x</sub> emissions was conducted for January, April,  
155 July, and October of 2016, representing the situations of the four seasons in the YRD  
156 region, and the horizontal resolution was 9×9 km. The inversed method assumed a  
157 nonlinear and variable correlation between NO<sub>x</sub> emissions and NO<sub>2</sub> TVCDs (Cooper  
158 et al., 2017), and the a posteriori daily emissions (top-down estimates) were calculated  
159 with the following equations:

$$160 \quad E_t = E_a \left( 1 + \frac{\Omega_o - \Omega_a}{\Omega_o} \beta \right) \quad (1)$$

$$161 \quad \frac{\Delta E}{E} = \beta \frac{\Delta \Omega}{\Omega} \quad (2)$$

162 where  $E_t$  and  $E_a$  represent the a posteriori and the a priori daily NO<sub>x</sub> emissions,  
163 respectively;  $\Omega_o$  and  $\Omega_a$  represent the observed and simulated NO<sub>2</sub> TVCDs,  
164 respectively;  $\beta$  represents the response coefficient of the simulated NO<sub>2</sub> TVCDs to a  
165 specific change in emissions, and was calculated based on the simulated changes in  
166 TVCDs ( $\Delta\Omega$ ) from a 10% changes in emissions ( $\Delta E$ ). For a given month, the a  
167 posteriori daily emissions were used as the a priori emissions of the next day, and the



168 monthly top-down estimate of the  $\text{NO}_x$  emissions was scaled from the average of the  
169 a posterior daily emissions of the last three days in the month, as the top-down  
170 estimate of daily  $\text{NO}_x$  emissions usually converged within a one-month simulation  
171 period (Zhao and Wang, 2009; Yang et al., 2019b).

172 The  $\text{NO}_2$  TVCDs were from OMI onboard the Aura satellite. It crosses the  
173 equator at 1:30 PM of local time. The horizontal resolution of OMI was  $24 \times 13$  km at  
174 nadir (Levelt et al., 2006), one of the finest resolutions available for  $\text{NO}_2$  TVCD  
175 observation before October 2017. We applied the Peking University Ozone  
176 Monitoring Instrument  $\text{NO}_2$  product (POMINO v1, Lin et al., 2014; Lin et al., 2015)  
177 to constrain the  $\text{NO}_x$  emissions. POMINO v1 modified the retrieval methodology of  
178 the Dutch Ozone Monitoring Instrument  $\text{NO}_2$  product (DOMINO v2) in China, and  
179 provided better linear correlation of  $\text{NO}_2$  TVCDs between the satellite and available  
180 ground-based observations with the multi-axis differential optical absorption  
181 spectroscopy (MAX-DOAS) (Lin et al., 2015). The original  $\text{NO}_2$  TVCDs from  
182 POMINO v1 (level 2) were resampled into an  $18 \times 18$  km grid system based on the  
183 area weight method, and then downsampled to  $9 \times 9$  km with the Kriging interpolation.  
184 As an example, the  $\text{NO}_2$  TVCDs for July 2016 in the YRD are shown in Figure S1 in  
185 the supplement, and larger TVCDs were found in the east-central YRD.

## 186 2.2 Model configuration

187 The Models-3 Community Multi-scale Air Quality (CMAQ) version 5.1 was  
188 used to conduct the inversed modeling of  $\text{NO}_x$  emission estimation and to simulate  
189 the ground-level concentrations of  $\text{NO}_2$ ,  $\text{O}_3$  and SIA. As a three-dimensional Eulerian  
190 model, CMAQ includes complex interactions of atmospheric chemistry and physics  
191 and is one of the most widely applied AQM to evaluate the sources and processes of  
192 air pollution in China (UNC, 2012; Xing et al., 2015; Zheng et al., 2017). As shown in  
193 Figure 1, the two nested modeling domains were applied with their horizontal  
194 resolutions set 27 and 9 km, respectively. The mother domain (D1,  $177 \times 127$  cells)  
195 included most parts of China, and the second (D2,  $118 \times 121$  cells) covered the YRD  
196 region. The model included 28 vertical layers and the height of the first layer (ground



197 layer) was approximately 60 m. The carbon bond gas-phase mechanism (CB05) and  
198 AERO6 aerosol module were used in the CMAQ. The initial concentrations and  
199 boundary conditions for the D1 were derived from the default clean profile, while  
200 those of D2 were extracted from the CMAQ Chemistry Transport Model (CCTM)  
201 outputs of its mother domain. The first 5 days of each simulated month were chosen  
202 as the spin-up period. Details on model configuration were described in Zhou et al.  
203 (2017) and Yang and Zhao (2019).

204 The Multi Resolution Emission Inventory for China (MEIC,  
205 <http://www.meicmodel.org/>) was applied as the initial input of anthropogenic  
206 emissions in D1 and D2, with an original horizontal resolution at  $0.1^{\circ} \times 0.1^{\circ}$ . In this  
207 study, the MEIC emissions from residential source were downscaled to the horizontal  
208 resolution of  $9 \times 9$  km based on the spatial density of population, and those from power,  
209 industry and transportation based on the spatial distribution of gross domestic product  
210 (GDP). The  $\text{NO}_x$  emissions from soil were originally obtained from Yienger and Levy  
211 (1995) and were doubled as advised by Zhao and Wang (2009). The emissions of Cl,  
212 HCl and lightning  $\text{NO}_x$  were collected from the Global Emissions Initiative (GEIA,  
213 Price et al., 1997). Biogenic emissions were derived from the Model Emissions of  
214 Gases and Aerosols from Nature developed under the Monitoring Atmospheric  
215 Composition and Climate project (MEGAN MACC, Sindelarova et al., 2014).

216 Meteorological fields were provided by the Weather Research and Forecasting  
217 Model (WRF) version 3.4, a state-of-the-art atmospheric modeling system designed  
218 for both numerical weather prediction and meteorological research (Skamarock et al.,  
219 2008). The simulated parameters from WRF for D2 in January, April, July and  
220 October of 2016 were compared with the observation dataset of US National Climate  
221 Data Center (NCDC), as summarized in Table S1 in the Supplement. The index of  
222 agreement (IOA) of wind speed for the four months between the two datasets was  
223 larger than 0.8. The Root Mean Square Error (RMSE) of wind directions for the four  
224 months was smaller than  $40^{\circ}$ , and the index of agreement (IOA) of temperature and  
225 Relative humidity between the two datasets was larger than 0.8 and 0.7, respectively.



226 The simulated meteorological parameters in D2 could reach the benchmarks derived  
227 from Emery et al. (2001) and Jiménez et al. (2006).

228 The hourly  $\text{NO}_2$  and  $\text{O}_3$  concentrations were observed at 230 state-operated  
229 stations of air quality monitoring in 41 cities within the YRD region, and they were  
230 applied to evaluate the model performance. Locations of the stations are indicated in  
231 Figure 1, and the observation data were derived from the China National  
232 Environmental Monitoring Center (<http://www.cnemc.cn/>). The observations of  $\text{SO}_4^{2-}$ ,  
233  $\text{NO}_3^-$  and  $\text{NH}_4^+$  (SNA) concentrations in  $\text{PM}_{2.5}$  for the YRD region during 2015-2017  
234 were collected and applied to evaluate the influence of the top-down estimation of  
235  $\text{NO}_x$  emissions on SNA simulation. In particular, the hourly SNA concentrations of  
236  $\text{PM}_{2.5}$  at Jiangsu Provincial Academy of Environmental Science, an urban site in the  
237 capital city of Jiangsu Province, Nanjing (JSPAES; Chen et al., 2019b), were  
238 observed with the Monitor for Aerosols and Gases in ambient Air (MARGA;  
239 Metrohm, Switzerland) for January, April, July and October 2016. Meanwhile, the  
240 daily average concentrations of SNA were also available from MARGA measurement  
241 for the four months at the Station for Observing Regional Processes and the Earth  
242 System, a suburban site in eastern Nanjing (SORPES; Ding et al., 2019). Besides, the  
243 seasonal average concentrations of SNA were available at another four sites in YRD,  
244 including the Nanjing University of Information Science & Technology site in  
245 Nanjing (NUIST, Zhang, 2017), and three sites respectively in the cities of Hangzhou  
246 (HZS; Li, 2018), Changzhou (CZS; Liu et al., 2018) and Suzhou (SZS; Wang et al.,  
247 2016). Details of the collected SNA measurement studies are summarized in Table S2  
248 in the supplement, and the locations of those sites are illustrated in Figure 1.

### 249 **2.3 Scenario setting of sensitivity analysis**

250 In general, there are two categories of chemical regimes (VOC-limited and  
251  $\text{NO}_x$ -limited) in  $\text{O}_3$  formation (Wang et al., 2009; Jin et al., 2017). In the VOC-limited  
252 regime, growth in  $\text{O}_3$  concentrations occurs with increased VOCs emissions and  
253 declined  $\text{NO}_x$  emissions, while the increased  $\text{NO}_x$  emissions result in enhancement of  
254  $\text{O}_3$  concentrations in the  $\text{NO}_x$ -limited regime. To explore the sources and potential



255 control approaches of O<sub>3</sub> pollution, the sensitivity of O<sub>3</sub> formation to its precursor  
256 emissions was analyzed with CMAQ modeling in the YRD region. As summarized in  
257 Table S3 in the supplement, eight cases were set besides the base scenario with the  
258 top-down NO<sub>x</sub> estimates for April 2016, the month with the largest O<sub>3</sub> concentration  
259 observed during the research period. Cases 1 and 2 reduced only the NO<sub>x</sub> emissions  
260 by 30% and 60%, and Cases 3 and 4 reduced only the VOC<sub>s</sub> emissions by 30% and  
261 60%, respectively. To explore the co-effect of VOCs and NO<sub>x</sub> emission controls on  
262 O<sub>3</sub> concentrations, Cases 5-8 with different reduction rates of VOCs and NO<sub>x</sub>  
263 emissions were designed. The emissions of NO<sub>x</sub> and VOCs in Case 5 were decreased  
264 by 30% and 60%, and in Case 6 by 60% and 30%, respectively. Both NO<sub>x</sub> and VOCs  
265 emissions were reduced 30% and 60% in Cases 7 and 8, respectively.

266 The response of SNA concentrations to the changes in precursor emissions was  
267 influenced by various factors including the abundance of NH<sub>3</sub>, atmospheric oxidation,  
268 and the chemical regime of O<sub>3</sub> formation (Wang et al., 2013; Cheng et al., 2016; Zhao  
269 et., 2020). To explore the sensitivity of SNA formation to its precursor emissions, four  
270 cases were set besides the base scenario for January 2016, the month with the largest  
271 observed SNA concentrations. As shown in Table S4 in the supplement, the emissions  
272 of NO<sub>x</sub>, SO<sub>2</sub> and NH<sub>3</sub> were reduced by 30% in Cases 9-11, respectively, and the  
273 emissions of NO<sub>x</sub>, SO<sub>2</sub> and NH<sub>3</sub> were simultaneously decreased by 30% in Case 12.

### 274 3. Results and discussion

#### 275 3.1 Evaluation of the bottom-up and top-down estimates of NO<sub>x</sub> emissions

276 Figure 2 compares the magnitude of the NO<sub>x</sub> emissions estimated based on the  
277 bottom-up (MEIC) and top-down methods by month in the YRD region. The  
278 top-down estimates were smaller than the bottom-up ones for all the concerned four  
279 months, and the average of the monthly NO<sub>x</sub> emissions were calculated at 260.0  
280 Gg/month for 2016 with the top-down method, 24% smaller than the bottom-up  
281 estimation. The comparison indicates a probable overestimation in NO<sub>x</sub> emissions  
282 with current bottom-up methodology, attributed partly to the insufficient consideration  
283 of the effect of recent control on emission abatement. Stringent measures have



284 gradually been conducted to improve the local air quality in the YRD region. For  
285 example, the “ultra-low” emission policy for power sector started in 2015, requiring  
286 the NO<sub>x</sub> concentration in the flue gas of coal-fired unit the same as that of gas-fired  
287 unit. The technology retrofitting on power units have been widely conducted,  
288 significant improving the NO<sub>x</sub> removal efficiencies of selective catalytic reduction  
289 (SCR) systems. Those detailed changes in emission control, however, could not be  
290 fully and timely incorporated into the national emission inventory that relied more on  
291 the routinely reported information and policy of environmental management over the  
292 country. With the on-line data from continuous emission monitoring systems (CEMS)  
293 incorporated, the NO<sub>x</sub> emissions from power sector were estimated to be 53% smaller  
294 than MEIC for the China in 2015 in our previous work (Zhang et al., 2019). The bias  
295 between the top-down and bottom-up estimates could be larger in earlier years and  
296 reduced more recently. According to Yang et al. (2019b) and Qu et al. (2017), for  
297 example, the top-down NO<sub>x</sub> emissions were 44% and 31% smaller than bottom-up  
298 ones for the YRD region and the whole China in 2012. Benefiting from the better data  
299 availability, the bottom-up inventory has been improved with the inclusion of more  
300 information on individual power and industrial plants for recent years (Zheng et al.,  
301 2018).

302 The differences in the spatial distribution of NO<sub>x</sub> emissions between the  
303 bottom-up and top-down estimates are illustrated by month for the YRD in Figure S2  
304 in the supplement. The top-down estimates were commonly smaller than the  
305 bottom-up ones in the east-central YRD with intensive manufacturing industry and  
306 population, and larger than those in most of Zhejiang Province with more hilly and  
307 suburban regions. The bias might result from following issues. From a bottom-up  
308 perspective, on one hand, more stringent control measures were preferentially  
309 conducted for power and industrial plants in regions with heavier air pollution like  
310 east-central YRD. As mentioned above, the effects of such actions were difficult to be  
311 fully tracked in the bottom-up inventory, leading to the overestimation in emissions  
312 for those regions. Due to the lack of precise locations of individual industrial plants  
313 (except for large point sources), moreover, the spatial allocation of the emissions



314 relied commonly on the densities of population and economy, assuming a strong  
315 correlation with emissions for them. Such assumption, however, would not still hold  
316 in recent years, as a number of factories in the relatively developed region were  
317 moved to the less developed suburban regions (e.g., southern Zhejiang) for both  
318 environmental and economic purposes. The insufficient consideration of the movings  
319 of emission sources was thus expected to result in overestimation in emissions for  
320 developed regions and underestimation for the less developed. On the other hand, the  
321 satellite-derived TVCDs were relatively small in southern Zhejiang (Fig. S1), and  
322 larger error in satellite retrieval and thereby emission constraining with the inversed  
323 modeling was expected.

324 Figure 3 illustrates the observed and simulated hourly  $\text{NO}_2$  concentrations using  
325 the bottom-up and top-down estimates of  $\text{NO}_x$  emissions in the CMAQ by month.  
326 The  $\text{NO}_2$  concentrations simulated with the bottom-up estimates were clearly larger  
327 than the observation in all the four concerned months, with the largest and smallest  
328 normalized mean bias (NMB) reaching 111% and 34 % for July and January,  
329 respectively. The result suggests again the overestimation in  $\text{NO}_x$  emissions in the  
330 current bottom-up inventory for the YRD. The model performance based on the  
331 top-down estimates was much better than that based on the bottom-up ones, indicating  
332 that the inversed modeling with satellite observation constraint effectively improved  
333 the estimation of  $\text{NO}_x$  emissions. The biggest improvement was found for July, with  
334 the NMB reduced from 111% to -0.4% and the NME reduced from 111% to 33%. As  
335 shown in Fig. 2, relatively big reduction from the bottom-up to top-down estimation  
336 in  $\text{NO}_x$  emissions was found for July compared to most of other months.

337 Scatter plots of the annual means of the observed and simulated surface  $\text{NO}_2$   
338 concentrations are shown in Figure S3 in the supplement. The slope between the  
339 observation and simulation with the top-down estimate (0.99) was much closer to 1  
340 than that with the bottom-up one (1.57), indicating clearly the advantage of the  
341 top-down method on the constraining of the magnitude of the total emissions in the  
342 YRD region. The difference in the two slopes implies that the surface  $\text{NO}_2$   
343 concentrations simulated with the bottom-up estimation were over 50% larger than



344 those based on top-down ones. As a comparison, the total emissions in the bottom-up  
345 inventory were only 30% larger than the top-down estimation for the whole YRD  
346 region. The larger overestimation in the concentrations than the emissions from the  
347 bottom-up inventory could result partly from the bias of the locations of  
348 state-operated ground observation sites. Most of those sites were located in the urban  
349 areas where excess emissions were allocated according to the high density of  
350 economy and population, and elevated concentrations were thus simulated compared  
351 to rural areas. The similar correlation coefficients (R) suggested that the spatial  
352 distribution of  $\text{NO}_x$  emissions was not greatly improved in the top-down estimation  
353 on an annual basis of urban observation. Uncertainty existed in the satellite  
354 observation: the NMB between  $\text{NO}_2$  TVCDs in POMINO and available ground-based  
355 MAX-DOAS observations was 21% in cloud-free days (Liu et al., 2019). Due mainly  
356 to the  $\text{NO}_x$  transport, moreover, a bias of 13%-33% on the spatial distribution of  
357 emissions was estimated for the inversed method at the horizontal resolution of 9 km  
358 or finer (Yang et al., 2019b). Inclusion of more available observation in rural areas  
359 helps improve the comprehensive evaluation of emission estimation.

360 Figure 4 illustrates the spatial distribution of monthly mean  $\text{NO}_2$  concentrations  
361 simulated based on the top-down estimates and the differences between the  
362 simulations with the top-down and bottom-up ones. The larger  $\text{NO}_2$  concentrations  
363 existed in the east-central YRD for all the months (left column in Fig. 5), and the  
364 difference in spatial distribution of  $\text{NO}_2$  concentrations (right column in Fig. 5) was  
365 similar with that in  $\text{NO}_x$  emissions (Fig. S2). Larger reduction in  $\text{NO}_2$  concentrations  
366 based on the top-down estimates was commonly found in east-central YRD, while the  
367 increased concentrations were found in most of Zhejiang.

### 368 **3.2 Evaluation of the $\text{O}_3$ simulation based on the top-down $\text{NO}_x$ estimates**

369 Figure 5 shows the observed and simulated hourly  $\text{O}_3$  concentrations based on  
370 the bottom-up and top-down estimates of  $\text{NO}_x$  emissions by month. Indicated by the  
371 smaller NMBs and NMEs, the model performance of  $\text{O}_3$  based on the top-down  
372 estimates was better than that based on the bottom-up ones for most months. It



373 suggests that the constrained  $\text{NO}_x$  emissions with satellite observation could play an  
374 important role on the improvement of  $\text{O}_3$  simulation. The largest improvement was  
375 found in January, for which the NMB and NME were changed from -44% and 49% to  
376 13% and 40%, respectively, attributed to the biggest change in  $\text{NO}_x$  emissions  
377 between the top-down and bottom-up estimates for the month. The worse  $\text{O}_3$   
378 modeling performance was found for July when the top-down estimate instead of the  
379 bottom-up one was applied in the simulation, indicated by the increased NMB and  
380 NME. Besides the changed  $\text{NO}_x$  emissions, the worse  $\text{O}_3$  simulation might result as  
381 well from the uncertainty in emissions of the volatile organic compounds (VOCs) and  
382 the chemical mechanism of AQM in summer. As suggested by Li (2019), the biogenic  
383 VOCs (BVOCs) emissions of the YRD region could be overestimated by 121% in  
384 summer attributed to ignoring the effect of droughts, and such overestimation might  
385 elevate the  $\text{O}_3$  concentrations in AQM. In order to explore the influence of uncertainty  
386 of BVOCs emissions on  $\text{O}_3$  model performance, we conducted an extra case in which  
387 the BVOCs emissions were cut by 50% in CMAQ. As shown in Figure S4 in the  
388 supplement, the NMB between the observed and simulated  $\text{O}_3$  based on the top-down  
389 estimate of  $\text{NO}_x$  emissions and the reduced BVOCs emissions declined 27% in July.  
390 A recent study conducted an intercomparison of surface-level  $\text{O}_3$  simulation from 14  
391 state-of-the-art chemical transport models, and implied that the larger overestimation  
392 of summer  $\text{O}_3$  than winter for eastern China resulted possibly from the uncertainty in  
393 the photochemical treatment in models (Li et al., 2019).

394 Table 1 summarizes the observed and simulated daily maximum 8-hour averaged  
395 (MDA8)  $\text{O}_3$  concentrations based on the bottom-up and top-down estimates of  $\text{NO}_x$   
396 emissions are summarized by month for the YRD region. The MDA8  $\text{O}_3$   
397 concentrations simulated with the top-down estimates were larger than those with the  
398 bottom-up ones, and were closer to the observation for most months. As most of the  
399 YRD was identified as the VOC-limited region (Li et al., 2012; Zhou et al., 2017), the  
400 reduced  $\text{NO}_x$  emissions with the top-down method enhanced the  $\text{O}_3$  levels in the  
401 AQM. Similar to the hourly concentrations, the most significant improvement for  
402 MDA8 was found in January, with the NMB and NME reduced from -35% and 39%



403 to 11% and 28%, respectively. Moreover, the improvement of April and October for  
404 MDA8 was larger than that for the hourly concentrations, indicating that the improved  
405 NO<sub>x</sub> emissions were more beneficial for the simulation of daytime peak O<sub>3</sub>  
406 concentrations in spring and winter. Figure 6 illustrates the spatial distribution of the  
407 monthly mean O<sub>3</sub> concentrations simulated based on the top-down NO<sub>x</sub> estimates and  
408 the differences between the simulations with the top-down and bottom-up estimates  
409 by month. In contrast to NO<sub>2</sub>, the smaller O<sub>3</sub> concentrations existed in the east-central  
410 YRD for most months, as it was identified as the VOC-limited region with relatively  
411 high NO<sub>2</sub> level. Larger O<sub>3</sub> concentrations were found for the surrounding regions in  
412 the YRD, e.g., southern Zhejiang, attributed partly to the relatively abundant BVOC  
413 emissions. An exception existed for July, with clearly larger O<sub>3</sub> concentrations in  
414 east-central YRD. With the largest population density and most developed economy in  
415 YRD, the area contains a large number of chemical industrial plants and solvent  
416 storage, transportation and usage (Zhao et al., 2017). High temperature in summer  
417 promoted the volatilization of chemical products and solvent, and thereby enhanced  
418 the seasonal VOCs emissions more significantly compared to other less developed  
419 YRD regions. Moreover, the lowest NO<sub>2</sub> concentration found in summer helped  
420 increase the O<sub>3</sub> concentration for the region (Gu et al., 2020). Regarding the  
421 simulation difference with two emission estimates, application of the top-down  
422 estimates instead of the bottom-up ones elevated the O<sub>3</sub> concentrations in most of the  
423 YRD region. In particular, the big reduction in NO<sub>x</sub> emissions for the east-central  
424 YRD (Figure S2) resulted in the more evident growth in O<sub>3</sub> concentrations, reflecting  
425 the negative effect of NO<sub>x</sub> abatement on O<sub>3</sub> pollution control in the VOC-limited  
426 regions.

### 427 **3.3 Evaluation of SIA simulation based on the top-down NO<sub>x</sub> estimates**

428 Shown in Table 2 is the comparison between the observed and simulated SNA  
429 (SO<sub>4</sub><sup>2-</sup>, NO<sub>3</sub><sup>-</sup> and NH<sub>4</sub><sup>+</sup>) concentrations by season. Larger observed and simulated  
430 SNA concentrations were found in winter and spring, and smaller were found in  
431 summer and autumn. For most seasons, the simulations of NO<sub>3</sub><sup>-</sup> concentrations were



432 moderately improved with the top-down estimates of  $\text{NO}_x$  emissions for all the  
433 concerned YRD cities, with an exception of Nanjing in autumn. The largest  
434 improvement was found in summer, with the mean bias between the simulation and  
435 observation reduced 35% for all the involved cities. Compared to the bottom-up  
436 inventory, the commonly smaller  $\text{NO}_x$  emissions in the top-down estimates limited  
437 the  $\text{NO}_2$  concentration and suppressed the formation of  $\text{NO}_3^-$ , while the enhanced  $\text{O}_3$   
438 from the reduced  $\text{NO}_x$  emissions promoted it (Cai et al., 2017; Huang et al., 2020). In  
439 summer, the former dominated the process with the most evident improvement in  $\text{NO}_2$   
440 simulation (Figure 3), thus the reduced  $\text{NO}_3^-$  concentrations that were closer to  
441 observation were simulated for all the cities.

442 The simulations with both top-down and bottom-up estimates of  $\text{NO}_x$  emissions  
443 underestimated the  $\text{NH}_4^+$  concentrations for most cases, and such underestimation was  
444 slightly corrected with the application of the top-down estimates except for summer.  
445 The average change in  $\text{NH}_4^+$  concentrations was 2.3%, much smaller than that of  
446  $\text{NO}_3^-$  at 14%. The moderate improvement in  $\text{NH}_4^+$  simulation with the reduced  $\text{NO}_x$   
447 emissions in the top-down estimates resulted partly from the enhancement of the  
448 simulated  $\text{O}_3$  concentrations and thereby the promoted  $\text{NH}_4^+$  formation. In summer,  
449 however, the significant drop in the simulated  $\text{NO}_2$  concentration was assumed to  
450 reduce the  $\text{NO}_3^-$  and  $\text{NH}_4^+$  formation, and to weaken the consistency between the  
451 simulated and observed  $\text{NH}_4^+$ . The difference between the simulated  $\text{SO}_4^{2-}$  with the  
452 bottom-up and top-down  $\text{NO}_x$  emission estimates were small for most seasons,  
453 implying a limited benefit of improved  $\text{NO}_x$  emissions on  $\text{SO}_4^{2-}$  modeling.

454 Figure 7 shows the differences in the spatial distribution of SNA concentrations  
455 simulated with the bottom-up and top-down estimates of  $\text{NO}_x$  emissions by month. In  
456 most of the region, the differences of  $\text{NO}_3^-$  concentrations were larger than those of  
457  $\text{NH}_4^+$  and  $\text{SO}_4^{2-}$  for all seasons, and they were mainly controlled by the changed  
458 ambient  $\text{NO}_2$  or  $\text{O}_3$  level. The difference in spatial pattern of  $\text{NO}_3^-$  was similar to that  
459 of  $\text{O}_3$  for January, and the larger growth attributed to the application of the top-down  
460 estimates was found in northern Anhui and eastern Zhejiang (Fig. 7a). The result  
461 implies that the change in  $\text{NO}_3^-$  concentration in winter could result partly from the



462 improved  $O_3$  simulation, i.e., the elevated  $O_3$  was an important reason for the  
463 enhanced the formation of SNA in winter (Huang et al., 2020). Similarly, the  
464 increased  $NO_3^-$  was found for more than half of the YRD region in April, along with  
465 the growth of  $O_3$  concentrations (Fig. 7d). For July, however, the difference in spatial  
466 pattern of  $NO_3^-$  (Fig. 7g) was similar with  $NO_2$  (Fig. 4g), and the larger reduction  
467 attributed to the application of the top-down estimates was found in northern YRD.  
468 The result suggests that the declining  $NO_x$  emissions and thereby  $NO_2$  concentration  
469 dominated the reduced  $NO_3^-$  formation in summer. In October, the growth in  $NO_3^-$   
470 concentrations was found again in most YRD when the top-down estimates were  
471 applied (Fig. 7j). The growth in the north resulted mainly from the increased  $O_3$  level,  
472 while that in the south was associated with the increased  $NO_2$ . The differences in  
473 spatial patterns of simulated  $NH_4^+$  concentrations were similar to those of  $NO_3^-$  for the  
474 four months, suggesting that the change in  $NH_4^+$  was associated with formation and  
475 decomposition of  $NH_4NO_3$ . However, the changes of spatial distribution of  $SO_4^{2-}$  were  
476 similar with those of  $O_3$  concentration. Since  $NH_4^+$  was preferred to react with  $SO_4^{2-}$   
477 rather than  $NO_3^-$  (Wang et al., 2013), the formation of  $SO_4^{2-}$  was mainly influenced by  
478 the atmospheric oxidizing capacity when only  $NO_x$  emissions were changed.

479 Figure 8 illustrates the observed and simulated hourly  $NO_3^-$  concentrations based  
480 on the bottom-up and top-down estimate of  $NO_x$  emissions by month at JSPAES. The  
481 NMBs and NMEs for simulation with the top-down emissions were smaller than those  
482 with bottom-up ones in January and July, implying the benefit of the improved  $NO_x$   
483 emissions on hourly  $NO_3^-$  concentration simulation in winter and summer. The best  
484 model performance with the top-down estimates was found in January, with the  
485 hourly variation commonly caught with AQM. However, the  $NO_3^-$  concentration was  
486 seriously overestimated and the model failed to catch the hourly variations in summer  
487 indicated by the large NMB and NME. As shown in Figure S5 in the supplement, both  
488 the  $NO_2$  and  $O_3$  concentrations at JSPAES were significantly overestimated for July  
489 except  $O_3$  with the bottom-up  $NO_x$  emission estimate, and it partly explained the  
490 elevated  $NO_3^-$  level from CMAQ simulation.

491 Figures S6 and S7 in the supplement compare the observed and simulated hourly



492 concentrations at JSPAES by month for  $\text{NH}_4^+$  and  $\text{SO}_4^{2-}$ , respectively. The NMBs and  
493 NMEs for  $\text{NH}_4^+$  simulation with the top-down estimates were smaller than those with  
494 the bottom-up ones for most months, while the changes in  $\text{SO}_4^{2-}$  concentration were  
495 small. The  $\text{NH}_4^+$  and  $\text{SO}_4^{2-}$  concentrations were largely underestimated with the  
496 top-down estimates in January, indicated by the NMB at -44% and -38%, respectively.  
497 Meanwhile, as shown in Figure S8 in the supplement, the  $\text{SO}_2$  concentrations were  
498 overestimated by 61% at the site. The results thus imply a great uncertainty in the  
499 gas-particle partitioning of  $(\text{NH}_4)_2\text{SO}_4$  formation in the model in winter, attributed  
500 probably to the missed oxidation mechanisms of  $\text{SO}_2$  (Chen et al., 2019c).

### 501 **3.4 Sensitivity analysis of $\text{O}_3$ and SNA formation in the YRD region**

502 Table 3 summarizes the relative changes in the simulated  $\text{O}_3$  concentrations for  
503 April 2016 in different cases. The mean  $\text{O}_3$  concentration would decline by 8.9% and  
504 19.5% with 30% and 60% VOCs emissions off (Cases 2 and 7), while it would  
505 increase by 14.2% and 23.7% with 30% and 60%  $\text{NO}_x$  emissions off (Cases 1 and 6),  
506 respectively. The result confirmed the VOC-limited regime of  $\text{O}_3$  formation in the  
507 YRD region: controlling VOCs emissions was an effective way to alleviate  $\text{O}_3$   
508 pollution, while reducing  $\text{NO}_x$  emissions alone would aggravate  $\text{O}_3$  pollution.

509 The growth of  $\text{O}_3$  concentrations was also found when the reduction rate of  $\text{NO}_x$   
510 emissions was equal to or larger than that of VOCs. The  $\text{O}_3$  concentration would  
511 increase by 7.1% and 14.5% respectively when both  $\text{NO}_x$  and VOCs emissions were  
512 reduced by 30% and 60% (Cases 3 and 8), and it would increase by 19.8% when  $\text{NO}_x$   
513 and VOCs emissions were respectively declined by 60% and 30% (Case 5). In  
514 contrast, small abatement of  $\text{O}_3$  concentrations (2.1%) was achieved from the 30%  
515 and 60% reduction of emissions respectively for  $\text{NO}_x$  and VOCs (Case 4), implying  
516 that the  $\text{O}_3$  level could be restrained when the reduction rate of VOCs was twice of or  
517 more than that of  $\text{NO}_x$ . To control the  $\text{O}_3$  pollution effectively and efficiently,  
518 therefore, the magnitude of VOCs and  $\text{NO}_x$  emission reduction should be carefully  
519 planned and implemented. In actual fact, controlling VOCs is more difficulty than  
520  $\text{NO}_x$ . Compared to  $\text{NO}_x$  that comes mainly from fossil fuel combustion (Zheng et al.,



521 2018), it is more complicated to identify the sources of specific VOCs species that are  
522 most active in  $O_3$  formation (Wei et al., 2014; Zhao et al., 2017). Moreover,  
523 substantial VOC emissions are from area or fugitive sources, for which the emission  
524 control technology can hardly be effectively applied. Therefore, it is a big challenge to  
525 control  $O_3$  pollution by reducing more VOCs than  $NO_x$ .

526 Figure 9 illustrates the differences in spatial patterns of the simulated monthly  
527 mean  $O_3$  concentrations between the base and sensitivity cases in April. The  $O_3$   
528 concentrations were expected to decline for the whole YRD region in the cases of  
529 30% and 60% VOCs emissions off (Fig. 9b and 9d), indicating the VOC-limited  
530 regime of  $O_3$  formation for the entire YRD. For other cases, the  $O_3$  concentrations  
531 were clearly elevated in the central-eastern YRD with relatively large population and  
532 developed industry, particularly for the cases with  $NO_x$  control only (Fig. 9a and 9c)  
533 or relatively large  $NO_x$  abatement together with VOC control (Fig. 9f and 9g). Even  
534 for the case with 60% of VOCs reduction and 30% of  $NO_x$  (Fig. 9h), there was still  
535 small increase in  $O_3$  concentration in central-eastern YRD, in contrast to the slight  $O_3$   
536 reduction found for most of YRD areas. Those results reveal the extreme difficulty in  
537  $O_3$  pollution control for the region. In southwestern Zhejiang, the  $O_3$  concentrations  
538 were found to decline in the cases with large abatement of  $NO_x$  emissions (Fig. 9b, 9f  
539 and 9g), suggesting a shifting from VOC-limited to  $NO_x$  limited region for the  $O_3$   
540 formation.

541 Table 4 summarizes the change in the simulated monthly means of SNA ( $NO_3^-$ ,  
542  $NH_4^+$  and  $SO_4^{2-}$ ) concentrations between the base case and sensitivity cases in January.  
543 The SNA concentrations were decreased in most cases, implying that the reduction in  
544 precursor emissions was useful for mitigating the SNA pollution. Compared to that of  
545 precursor emissions, however, the reduction rate of SNA was much smaller attributed  
546 to the strong nonlinearity of SNA formation. The largest reductions were found at  
547 11.7% and 12.4% when emissions of  $NH_3$  and all the three precursors were decreased  
548 by 30% (Cases 11 and 12), respectively. In contrast, the SNA concentrations declined  
549 slightly by 1% and increased by 0.5% when  $NO_x$  and  $SO_2$  emissions were reduced by  
550 30% (Cases 9 and 10), respectively. The results suggest that most of YRD was in an



551 NH<sub>3</sub>-neutral or even NH<sub>3</sub>-poor condition in winter, consistent with the judgment  
552 through AQM based on an updated NH<sub>3</sub> emission inventory (Zhao et al., 2020), as the  
553 NH<sub>3</sub> volatilization in winter was much smaller than other seasons. Reducing NH<sub>3</sub>  
554 emissions was the most efficient way to control SNA pollution for the region in winter.  
555 In Case 11 with NH<sub>3</sub> control only, the reduced NO<sub>3</sub><sup>-</sup> and NH<sub>4</sub><sup>+</sup> were much larger than  
556 that of SO<sub>4</sub><sup>2-</sup>. As NH<sub>3</sub> reacted with SO<sub>2</sub> prior to NO<sub>x</sub>, NH<sub>4</sub>NO<sub>3</sub> was assumed easier to  
557 decompose than (NH<sub>4</sub>)<sub>2</sub>SO<sub>4</sub> when NH<sub>3</sub> emissions were reduced. The growth of NO<sub>3</sub><sup>-</sup>  
558 concentrations was found for Case 10 (SO<sub>2</sub> control only), since the free NH<sub>3</sub> from the  
559 reduced SO<sub>2</sub> emissions could react with NO<sub>x</sub> in the NH<sub>3</sub>-poor condition. Similarly, the  
560 SO<sub>4</sub><sup>2-</sup> concentrations increased for Case 9 (NO<sub>x</sub> control only), as the elevated O<sub>3</sub>  
561 attributed to the reduction of NO<sub>x</sub> emissions promoted the SO<sub>4</sub><sup>2-</sup> formation.

562

#### 4. Summary

563 From a “top-down” perspective, we have estimated the monthly NO<sub>x</sub> emissions  
564 for the YRD region in 2016, based on the nonlinear inversed modeling and NO<sub>2</sub>  
565 TVCDs from POMINO, and the bottom-up and top-down estimates of NO<sub>x</sub> emissions  
566 were evaluated with AQM and ground NO<sub>2</sub> observation. Due to insufficient  
567 consideration of improved controls on power and industrial sources, the NO<sub>x</sub>  
568 emissions were probably overestimated in current bottom-up inventory (MEIC),  
569 resulting in significantly higher simulated NO<sub>2</sub> concentrations than the observation.  
570 The simulated NO<sub>2</sub> concentrations with the top-down estimates were closer to the  
571 observation for all the four seasons, suggesting the improved emission estimation with  
572 satellite constraint. Improved O<sub>3</sub> and SNA simulations with the top-down NO<sub>x</sub>  
573 estimates for most months indicate the importance role of precursor emission  
574 estimation on secondary pollution modeling for the region. Through the sensitivity  
575 analysis of O<sub>3</sub> formation, the mean O<sub>3</sub> concentrations were found to decrease for most  
576 YRD when only VOCs emissions were reduced or the reduced rate of VOCs was  
577 twice of NO<sub>x</sub>, and the result indicates the effectiveness of controlling VOCs  
578 emissions on O<sub>3</sub> pollution abatement for the region. For part of southern Zhejiang,  
579 however, the O<sub>3</sub> concentrations were simulated to decline with the reduced NO<sub>x</sub>



580 emissions, implying the shifting from VOC-limited to NO<sub>x</sub>-limited region. Compared  
581 to reducing NO<sub>x</sub> or SO<sub>2</sub> only, larger reduction in SNA concentrations was found when  
582 30% of emissions were cut for NH<sub>3</sub> or all the three precursors (NO<sub>2</sub>, NH<sub>3</sub> and SO<sub>2</sub>).  
583 The result suggests that reducing NH<sub>3</sub> emissions was crucial to alleviate SNA  
584 pollution of YRD in winter.

585 Limitations remain in this study. Due to the limited horizontal resolution of OMI,  
586 relatively big bias existed in the spatial distribution of the constrained NO<sub>x</sub> emissions  
587 at the regional scale compared to national or continental one, and the uncertainty  
588 could exceed 30% for the YRD region (Yang et al., 2019b). Therefore the  
589 improvement on the top-down estimates of NO<sub>x</sub> emissions can be expected when the  
590 more advanced and reliable products of satellite observation get available at finer  
591 horizontal resolution (e.g., TROPOspheric Monitoring Instrument, TROPOMI).  
592 Besides, more SNA observations from on-line measurement are recommended for a  
593 better space coverage and temporal resolution, to explore more carefully the response  
594 of SNA to the changes in emissions of NO<sub>x</sub> and other precursors.

595

#### 596 **Data availability**

597 All data in this study are available from the authors upon request.

598

#### 599 **Author contributions**

600 YY developed the strategy and methodology of the work and wrote the draft. YZ  
601 improved the methodology and revised the manuscript. LZ provided useful comments  
602 on the methodology. JZ and XH provided observation data of secondary inorganic  
603 aerosols. XZ, YZ, MX and YL provided comments on air quality modeling.

604

#### 605 **Competing interests**

606 The authors declare that they have no conflict of interest.

607



608

### Acknowledgements

609 This work was sponsored by Natural Science Foundation of China (91644220 and  
610 41575142) and the National Key Research and Development Program of China  
611 (2017YFC0210106). We would also like to thank Tsinghua University for the free use  
612 of national emissions data (MEIC), and Peking University for the support of satellite  
613 data (POMINO v1).  
614

615

### References

- 616 Cai, S., Wang, Y., Zhao, B., Chang, X., Hao, J. M.: The impact of the “Air Pollution  
617 Prevention and Control Action Plan” on PM<sub>2.5</sub> concentrations in Jing-Jin-Ji region  
618 during 2012–2020, *Sci. Total Environ.*, 580, 197–209, 2017.
- 619 Chen, D., Tian, X., Lang J., Zhou, Y., Li, Y., Guo, X. Wang, W., Liu, B.: The impact  
620 of ship emissions on PM<sub>2.5</sub> and the deposition of nitrogen and sulfur in Yangtze River  
621 Delta, China, *Sci. Total Environ.*, 649, 1609–1619, 2019a.
- 622 Chen, D., Zhao, Y., Lyu, R., Wu, R., Dai, L., Zhao, Y., Chen, F., Zhang, J., Yu, H.,  
623 Guan, M.: Seasonal and spatial variations of optical properties of light absorbing  
624 carbon and its influencing factors in a typical polluted city in Yangtze River Delta,  
625 China. *Atmos. Environ.*, 199, 45–54, 2019b.
- 626 Chen, L., Gao, Y., Zhang, M., Fu, J. S., Kurokawa, J. I.: Mics-Asia III: multi-model  
627 comparison and evaluation of aerosol over East Asia, *Atmos. Chem. Phys.*, 19,  
628 11911–11937, 2019c.
- 629 Cheng, Y. F., Zheng, G. J., Wei, C., Mu, Q., Zheng, B., Wang, Z. B., Gao, M., Zhang,  
630 Q., He, K. B., Carmichael, G., Pöschl, U., Su H.: Reactive nitrogen chemistry in  
631 aerosol water as a source of sulfate during haze events in China, *Sci. Adv.*,  
632 2(e1601530), 1–11, 2016.
- 633 Cooper, M., Martin, R.V., Padmanabhan, A., Henze, D.K.: Comparing mass balance  
634 and adjoint methods for inverse modeling of nitrogen dioxide columns for global  
635 nitrogen oxide emissions, *J. Geophys. Res.: Atmosphere*, 122, 4718–4734, 2017.
- 636 de Foy, B., Lu, Z., Streets, D.G., Lamsal, L.N., Duncan., B.N.: Estimates of power  
637 plant NO<sub>x</sub> emissions and lifetimes from OMI NO<sub>2</sub> satellite retrievals, *Atmos.*  
638 *Environ.*, 116, 1–11, 2015.
- 639 Ding, A., Huang, X., Nie, W., Chi, X., Xu, Z., Zheng, L., Xu, Z., Xie, Y., Qi, X., Shen,  
640 Y., Sun, P., Wang, J., Wang, L., Sun, J., Yang, X., Qin, W., Zhang, X., Cheng, W., Liu,  
641 W., Pan, L., Fu, C.: Significant reduction of PM<sub>2.5</sub> in eastern China due to  
642 regional-scale emission control: evidence from SORPES in 2011–2018, *Atmos. Chem.*  
643 *Phys.*, 19, 11791–11801, 2019.



- 644 Ding, J.Y., Miyazaki, K., van der, R.J., Mijling, B., Kurokawa, J., Cho, S.Y., Greet  
645 Janssens-Maenhout, G., Zhang, Q., Liu, F., Levelt, P.F.: Intercomparison of NO<sub>x</sub>  
646 emission inventories over East Asia, *Atmos. Chem. Phys.*, 17, 10125-10141, 2017.
- 647 Emery, C., Tai, E., Yarwood, G.: Enhanced meteorological modeling and  
648 performance evaluation for two Texas episodes, Report to the Texas Natural  
649 Resources Conservation Commission, prepared by ENVIRON, International Corp,  
650 Novato, CA, 2001.
- 651 Granier, C., Bessagnet, B., Bond, T., Angiola A.D., van der G.H.D., Frost G.J., Heil  
652 A., Kaiser J.W., Kinne S., Klimont Z., Kloster S., Lamarque J.F., Lioussé C., Masui T.,  
653 Meleux, F., Mieville, A., Ohara, T., Raut, J.C., Riahi, K., Schultz, M.G., Smith, S.J.,  
654 Thompson, A., van Aardenne, J., van der Werf, G.R., van Vuuren, D.P.: Evolution of  
655 anthropogenic and biomass burning emissions of air pollutants at global and regional  
656 scales during the 1980–2010 period. *Climatic Change*, 109, 163-190, 2011.
- 657 Gu, D.S., Wang, Y.X., Smeltzer, C., Boersma, K.F.: Anthropogenic emissions of NO<sub>x</sub>  
658 over China: Reconciling the difference of inverse modeling results using GOME-2  
659 and OMI measurements, *J. Geophys. Res.: Atmosphere*, 119, 7732-7740, 2014.
- 660 Gu, Y. X., Li, K., Xu, J. M., Liao, H., Zhou, G. Q.: Observed dependence of surface  
661 ozone on increasing temperature in Shanghai, China, *Atmos. Environ.*, 221, 1–10,  
662 2020.
- 663 Huang, X., Ding, A. J., Gao, J., Zheng, B., Zhou, D. R., Qi, X. M., Tang, R., Ren, C.  
664 H., Nie, W., Chi, X. G., Wang, J. P., Xu, Z., Chen, L. D., Li, Y. Y., Che, F., Pang, N. N.,  
665 Wang, H. K., Tong, D., Qin, W., Cheng, W., Liu, W. J., Fu, Q. Y., Chai, F. H., Davis, S.  
666 J., Zhang, Q., He K. B.: Enhanced secondary pollution offset reduction of primary  
667 emissions during COVID-19 lockdown in China, *Natl. Sci. Rev.*, nwa137,  
668 <https://doi.org/10.1093/nsr/nwaa137>, 2020.
- 669 Jena, C., Ghude, S. D, Beig, G., Chate, D. M., Kumar, R, Pfister, G. G., Lal, D. M.,  
670 Surendran, D. E., Fadnavis, S., van der A, R. J.: Inter-comparison of different NO<sub>x</sub>  
671 emission inventories and associated variation in simulated surface ozone in Indian  
672 region, *Atmos. Environ.*, 17, 61-73, 2014.
- 673 Jiménez, P., Jorba, O., Parra R., Baldasano, J. M.: Evaluation of  
674 MM5-EMICAT2000-CMAQ performance and sensitivity in complex terrain:  
675 High-resolution application to the northeastern Iberian Peninsula, *Atmos. Environ.*, 40,  
676 5056-5072, 2006.
- 677 Jin, X. M., Fiore, A. M., Murray, L. T., Valin, L. C., Lamsal, L. N., Duncan, B.,  
678 Boersma, K. F., De Smedt, I., Abad, G. G., Chance, K., Tonnesen, G. S.: Evaluating a  
679 space-based Indicator of surface ozone-NO<sub>x</sub>-VOC sensitivity over midlatitude source  
680 regions and application to decadal trends, *J. Geophys. Res.-Atmos.*, 122,  
681 10231–10253, 2017.



- 682 Kong, H., Lin J.T., Zhang, R.X., Liu, M.Y., Weng, H.J., Ni, R.J., Chen, L.L., Wang,  
683 J.X., Zhang, Q.: High-resolution ( $0.05^\circ \times 0.05^\circ$ ) NO<sub>x</sub> emissions in the Yangtze River  
684 Delta inferred from OMI, *Atmos. Chem. Phys.*, 19, 12835-12856, 2019.
- 685 Kurokawa, J.I., Yumimoto, K., Uno, I., Ohara, T.: Adjoint inverse modeling of NO<sub>x</sub>  
686 emissions over eastern China using satellite observations of NO<sub>2</sub> vertical column  
687 densities, *Atmos. Environ.*, 43, 1878-1887, 2009.
- 688 Levelt, P.F., Hilsenrath, E., Leppelmeier, G.W., van den Oord, G.H.J., Bhartia, P.K.,  
689 Tamminen, J., de Haan, J.F., Veefkind, J.P.: Science objectives of the Ozone  
690 Monitoring Instrument, *IEEE T. Geosci. Remote*, 44, 1199-1208, 2006.
- 691 Li, L.: The numerical simulation of comprehensive air pollution characteristics in a  
692 typical city-cluster, Doctoral dissertation, Shanghai University, Shanghai, China,  
693 2012.
- 694 Li, L.: Application of new generation natural source emission model in Yangtze River  
695 Delta and its influence on SOA and O<sub>3</sub> (in Chinese), The 4th application technology  
696 seminar on air pollution source emission inventory in China, Nanjing, China,  
697 September 18-19, 2019.
- 698 Li, J., Nagashima, T., Kong, L., Ge, B., Yamaji, K., Fu, J.S., Wang, X., Fan, Q.,  
699 Itahashi, S., Lee, H.J., Kim, C.H., Lin, C.Y., Zhang, M., Tao, Z., Kajino, M., Liao, H.,  
700 Li, M., Woo, J.H., Kurokawa, J., Wang, Z., Wu, Q., Akimoto, H., Carmichael, G. R.,  
701 and Wang, Z.: Model evaluation and intercomparison of surface-level ozone and  
702 relevant species in East Asia in the context of MICS-Asia Phase III – Part 1:  
703 Overview, *Atmos. Chem. Phys.*, 19, 12993-13015, 2019.
- 704 Li, Z.: Seasonal pollution characteristics and cytotoxicity of PM<sub>2.5</sub> in district of  
705 Hangzhou City (in Chinese), Master thesis, Zhejiang University, Hangzhou, China,  
706 2018.
- 707 Lin, J. T., Martin, R. V., Boersma, K. F., Sneep, M., Stammes, P., Spurr, R., Wang, P.,  
708 Van Roozendaal, M., Clémer, K., Irie, H.: Retrieving tropospheric nitrogen dioxide  
709 from the Ozone Monitoring Instrument: Effects of aerosols, surface reflectance  
710 anisotropy, and vertical profile of nitrogen dioxide, *Atmos. Chem. Phys.*, 14,  
711 1441-1461, 2014.
- 712 Lin, J. T., Liu, M. Y., Xin, J. Y., Boersma, K. F., Spurr, R., Martin, R., Zhang, Q.:  
713 Influence of aerosols and surface reflectance on satellite NO<sub>2</sub> retrieval: seasonal and  
714 spatial characteristics and implications for NO<sub>x</sub> emission constraints, *Atmos. Chem.*  
715 *Phys.*, 15, 11217-11241, 2015.
- 716 Liu, F., van der, A R., Eskes, H., Ding, J., Mijling, B.: Evaluation of modeling NO<sub>2</sub>  
717 concentrations driven by satellite-derived and bottom-up emission inventories using  
718 in situ measurements over China, *Atmos. Chem. Phys.*, 18, 4171-4186, 2018.



- 719 Liu, J. S., Gu, Y., Ma, S. S., Su, Y. L., Ye, Z. L.: Day-night differences and source  
720 apportionment of inorganic components of PM<sub>2.5</sub> during summer-winter in  
721 Changzhou city (in Chinese), *Environ. Sci.*, 39, 980-989, 2018.
- 722 Liu, M.Y., Lin, J.T., Boersma, K.F., Pinaridi, G., Wang, Y., Chimot, J., Wagner, T., Xie,  
723 P., Eskes, H., Van Roozendaal, M., Hendrick, F., Wang, P., Wang, T., Yan, Y.Y., Chen,  
724 L.L., Ni, R.J.: Improved aerosol correction for OMI tropospheric NO<sub>2</sub> retrieval over  
725 East Asia: constraint from CALIOP aerosol vertical profile, *Atmos. Measure. Tec.*, 12,  
726 1-21, 2019.
- 727 Martin, R.V., Jacob, D.J., Chance, K., Kurosu, T.P., Palmer, P.I., Evans, M.J.: Global  
728 inventory of nitrogen oxide emissions constrained by space-based observations of  
729 NO<sub>2</sub> columns, *J. Geophys. Res.*, 108, 1-12, 2003.
- 730 Ming, L. L., Jin, L., Li J., Yang, W. Y., Liu, D., Zhang, G., Wang, Z. F., Lia, X. D.:  
731 PM<sub>2.5</sub> in the Yangtze River Delta, China: Chemical compositions, seasonal variations,  
732 and regional pollution events, *Environ. Pollut.*, 223, 200-212, 2017.
- 733 Ministry of Environmental protection of the People's Republic of China (MEPPRC):  
734 Chinese Environmental Situation Communique in 2016, Beijing, 2017.
- 735 Miyazaki, K., Eskes, H. J., and Sudo, K.: Global NO<sub>x</sub> emission estimates derived  
736 from an assimilation of OMI tropospheric NO<sub>2</sub> columns, *Atmos. Chem. Phys.*, 12,  
737 2263–2288, 2012.
- 738 Price, C., Penner, J., Prather, M.: NO<sub>x</sub> from lightning, Part I: Global distribution  
739 based on lightning physics, *J. Geophys. Res.: Atmospheres*, 102, D5, 1-5, 1997.
- 740 Qu, Z., Henze, D.K., Capps, S.L., Wang, Y., Xu, X., Wang, J., Keller, M., Monthly  
741 top-down NO<sub>x</sub> emissions for China (2005–2012): A hybrid inversion method and  
742 trend analysis, *J. Geophys. Res.: Atmosphere*, 122, 4600-4625, 2017.
- 743 Saikawa, E., Kim, H., Zhong, M., Zhao, Y., Janssens-Maenhout, G., Kurokawa, J.,  
744 Klimont, Z., Wagner, F., Naik, V., Horowitz, L.W., Zhang, Q.: Comparison of  
745 emissions inventories of anthropogenic air pollutants and greenhouse gases in China,  
746 *Atmos. Chem. Phys.*, 17, 6393-6421, 2017.
- 747 Sindelarova, K., Granier, C., Bouarar, I., Guenther, A., Tilmes, S., Stavrou, T.,  
748 Müller, J.F., Kuhn, U., Stefani, P., Knorr, W.: Global data set of biogenic VOC  
749 emissions calculated by the MEGAN model over the last 30 years, *Atmos. Chem.*  
750 *Phys.*, 14, 9317–9341, 2014.
- 751 Skamarock, W. C., Klemp, J. B., Dudhia, J., Gill, D. O., Barker, D. M., Duda, M. G.,  
752 Huang, X.-Y., Wang, W., Powers, J. G.: A Description of the Advanced Research WRF  
753 Version 3. NCAR Tech. Note NCAR/TN-475+STR, 113 pp.doi:10.5065/D68S4MVH,  
754 2008.
- 755 University of North Carolina at Chapel Hill (UNC): Operational Guidance for the  
756 Community Multiscale Air Quality (CMAQ) Modeling System Version 5.0 (February



- 757 2012 Release), available at <http://www.cmaq-model.org> (last access: 10 June 2020),  
758 2012.
- 759 Visser, A. J., Boersma, K. F., Ganzeveld, L. N., Krol, M. C.: European NO<sub>x</sub>  
760 emissions in WRF-Chem derived from OMI: impacts on summertime surface ozone,  
761 *Atmos. Chem. Phys.*, 19, 11821-11841, 2019.
- 762 Wang, N. F., Chen, Y., Hao, Q. J., Wang, H. B., Yang, F. M., Zhao, Q., Bo, Y., He, K.  
763 B., Yao, Y. G.: Seasonal variation and source analysis on water-soluble ion of PM<sub>2.5</sub> in  
764 Suzhou (in Chinese), *Environ. Sci.*, 37, 4482-4489, 2016.
- 765 Wang, N., Lyu, X., Deng, X., Huang, X., Jiang, F., Ding, A.: Aggravating O<sub>3</sub> pollution  
766 due to NO<sub>x</sub> emission control in eastern China, *Sci. Total Environ.*, 677, 732-744,  
767 2019.
- 768 Wang, X., Zhang, Y., Hu, Y., Zhou, W., Lu, K., Zhong, L., Zeng, L., Shao, M., Hu, M.,  
769 Russell, A. G.: Process analysis and sensitivity study of regional ozone formation over  
770 the Pearl River Delta, China, during the PRIDE-PRD2004 campaign using the CMAQ  
771 model, *Atmos. Chem. Phys.*, 9, 635-645, 2009.
- 772 Wang, Y., Zhang, Q. Q., He, K., Zhang, Q., Chai, L.: Sulfate-nitrate-ammonium  
773 aerosols over China: response to 2000-2015 emission changes of sulfur dioxide,  
774 nitrogen oxides, and ammonia, *Atmos. Chem. Phys.*, 13, 2635-2652, 2013.
- 775 Wei, W., Wang, S. X., Hao, J. M., Cheng, S. Y.: Trends of Chemical Speciation  
776 Profiles of Anthropogenic Volatile Organic Compounds Emissions in China,  
777 2005-2020, *Front. Env. Sci. Eng. in China*, 8: 27-41, 2014.
- 778 Xing, J., Mathur, R., Pleim, J., Pouliot, G.: Observations and modeling of air quality  
779 trends over 1990-2010 across the Northern Hemisphere: China, the United States and  
780 Europe, *Atmos. Chem. Phys.*, 15, 2723-2747, 2015.
- 781 Yang, Y., Zhao, Y.: Quantification and evaluation of atmospheric pollutant emissions  
782 from open biomass burning with multiple methods: A case study for Yangtze River  
783 Delta region, China, *Atmos. Chem. Phys.*, 19, 327-348, 2019.
- 784 Yang, Y., Zhao, Y., Zhang, L.: Evaluating the influence of satellite observation on  
785 inverting NO<sub>x</sub> emission at regional scale. *Int. Arch. Photogramm. Remote Sens.*  
786 *Spatial Inf. Sci.*, XLII-3/W9, 211-217, 2019a.
- 787 Yang Y., Zhao Y., Zhang L., Lu Y.: Evaluating the methods and influencing factors of  
788 satellite-derived estimates of NO<sub>x</sub> emissions at regional scale: A case study for  
789 Yangtze River Delta, China. *Atmos. Environ.*, 219, 1-12, 2019b.
- 790 Yienger, J.J., Levy, II H.: Empirical model of global soil biogenic NO<sub>x</sub> emissions, *J.*  
791 *Geophys. Res.*, 100, 11447-11464, 1995.
- 792 Zhang, Y, Bo, X, Zhao, Y, Nielsen, C.P.: Benefits of current and future policies on  
793 emission reduction from China's coal-fired power sector indicated by continuous  
794 emission monitoring, *Environ. Pollut.*, 251: 415-424, 2019.



- 795 Zhang, Y. Y.: Characteristic of water-soluble ions in PM<sub>2.5</sub> in the northern suburb of  
796 Nanjing based on on-line monitoring (in Chinese), Master thesis, Nanjing University  
797 of Information Science & Technology, Nanjing, China, 2017.
- 798 Zhao, C., and Wang, Y. X.: Assimilated inversion of NO<sub>x</sub> emissions over East Asia  
799 using OMI NO<sub>2</sub> column measurements. *Geophys. Res. Lett.*, 2009, 36( L06805): 1-5.
- 800 Zhao, Y., Mao, P., Zhou, Y., Yang, Y., Zhang, J., Wang, S., Dong, Y., Xie, F., Yu, Y., Li,  
801 W.: Improved provincial emission inventory and speciation profiles of anthropogenic  
802 non-methane volatile organic compounds: a case study for Jiangsu, China, *Atmos.*  
803 *Chem. Phys.*, 17, 7733-7756, 2017.
- 804 Zhao, Y., Yuan, M. C., Huang, X., Chen, F., Zhang, J.: Quantification and evaluation  
805 of atmospheric ammonia emissions with different methods: A case study for the  
806 Yangtze River Delta region, China, *Atmos. Chem. Phys.*, 20, 4275-4294, 2020.
- 807 Zheng, B., Tong, D., Li, M., Liu, F., Hong, C., Geng, G., Li, H., Li, X., Peng, L., Qi, J.,  
808 Yan, L., Zhang, Y., Zhao, H., Zheng, Y., He, K., and Zhang, Q.: Trends in China's  
809 anthropogenic emissions since 2010 as the consequence of clean air actions, *Atmos.*  
810 *Chem. Phys.*, 18, 14095–14111, 2018.
- 811 Zhou, Y. D., Zhao, Y. D., Mao, P., Zhang, Q., Zhang, J., Qiu, L.P., Yang, Y.:  
812 Development of a high-resolution emission inventory and its evaluation and  
813 application through air quality modeling for Jiangsu Province, China, *Atmos. Chem.*  
814 *Phys.*, 17, 211-233, 2017.
- 815 Zyrichidou, I., Koukouli, M.E., Balis, D., Markakis, K., Poupkou, A., Katragkou, E.,  
816 Kioutsioukis, I., Melas, D., Boersma, K.F., van Roozendaal, M.: Identification of  
817 surface NO<sub>x</sub> emission sources on a regional scale using OMI NO<sub>2</sub>, *Atmos. Environ.*,  
818 101, 82–93, 2015.



## FIGURE CAPTIONS

**Figure 1.** The modeling domain and locations of meteorological and air quality monitoring sites. The map data provided by Resource and Environment Data Cloud Platform are freely available for academic use (<http://www.resdc.cn/data.aspx?DATAID=201>), © Institute of Geographic Sciences & Natural Resources Research, Chinese Academy of Sciences.

**Figure 2.** The bottom-up and top-down estimates of  $\text{NO}_x$  emissions by month for the YRD region in 2016.

**Figure 3.** The observed and simulated hourly  $\text{NO}_2$  concentrations based on the bottom-up and top-down  $\text{NO}_x$  emissions for January, April, July and October 2016.

**Figure 4.** The spatial distribution of the simulated monthly mean  $\text{NO}_2$  concentration with the top-down estimates and differences between the simulations with the top-down and bottom-up  $\text{NO}_x$  emissions in January, April, July and October 2016 (top-down minus bottom-up).

**Figure 5.** The observed and simulated hourly  $\text{O}_3$  concentrations with the bottom-up and top-down  $\text{NO}_x$  emission estimates for January, April, July and October 2016.

**Figure 6.** The spatial distribution of the simulated monthly mean  $\text{O}_3$  concentration with the top-down  $\text{NO}_x$  estimates and the spatial differences between the simulations with the top-down and bottom-up  $\text{NO}_x$  emissions in January, April, July and October 2016 (top-down minus bottom-up).

**Figure 7.** The spatial differences between the simulated SNA concentrations with the bottom-up and top-down  $\text{NO}_x$  emission estimates for January, April, July and October 2016 (top-down minus bottom-up).

**Figure 8.** The observed and simulated hourly  $\text{NO}_3^-$  concentrations with the bottom-up and top-down  $\text{NO}_x$  emission estimates for January, April, July and



**October 2016 at JSPEAS.**

**Figure 9. The spatial differences of monthly mean O<sub>3</sub> concentrations between the simulations based on base case (top-down estimates) and sensitivity cases in April 2016 (sensitivity case minus base case).**



## TABLES

**Table 1. The model performance statistics of daily maximum 8-hour averaged (MDA8) O<sub>3</sub> concentrations in January, April, July and October 2016 with the bottom-up and top-down NO<sub>x</sub> emissions.**

Month	Emission input	Observed ( $\mu\text{g}/\text{m}^3$ )	Simulated ( $\mu\text{g}/\text{m}^3$ )	NMB	NNE
January	Bottom-up	50.6	33.0	-34.8%	38.6%
	Top-down		56.3	11.3%	27.7%
April	Bottom-up	101.5	87.2	-14.1%	20.2%
	Top-down		108.5	6.9%	16.1%
July	Bottom-up	107.4	117.3	9.2%	15.7%
	Top-down		140.7	31.0%	31.0%
October	Bottom-up	65.9	53.9	-18.3%	23.2%
	Top-down		73.4	11.3%	21.7%



**Table 2.** Comparison of observed and simulated  $\text{NO}_3^-$ ,  $\text{NH}_4^+$  and  $\text{SO}_4^{2-}$  concentrations by site and season in 2016 (unit:  $\mu\text{g}/\text{m}^3$ ). The information of SNA observation sites is provided in Table S2 in the supplement. BU and TD indicate the CMAQ modeling with the bottom-up and top-down estimate of  $\text{NO}_x$  emissions, respectively.

	Spring			Summer			Autumn			Winter		
	$\text{NO}_3^-$	$\text{NH}_4^+$	$\text{SO}_4^{2-}$									
JSPAES	19.1	16.5	12.7	5.7	9.3	10.5	10.3	6.1	9.7	31.1	16.5	20.3
CMAQ (BU)	20.7	8.5	12.0	14.4	6.0	9.1	10.9	5.0	9.0	25.6	9.3	12.8
CMAQ (TD)	22.3	9.0	12.2	11.8	5.4	9.5	11.6	5.2	9.1	26.2	9.4	12.8
SORPES	14.1	8.6	13.2	7.5	6.6	11.5	8.8	5.2	8.3	23.0	13.4	15.7
CMAQ (BU)	18.5	7.3	8.0	12.2	4.3	5.2	9.3	4.0	5.4	23.6	8.7	10.9
CMAQ (TD)	18.0	7.0	7.4	8.3	3.7	5.0	9.8	4.2	5.4	23.6	8.8	10.1
NUIST	16.9	11.0	15.9	6.8	7.1	13.1	N/A	N/A	N/A	20.9	14.3	16.8
CMAQ (BU)	20.0	7.9	9.9	14.0	5.8	7.5				24.3	9.0	11.3
CMAQ (TD)	21.8	8.5	9.9	11.8	5.3	7.8				24.6	9.1	11.3
HZS	19.9	6.6	19.9	1.9	2.8	6.2	12.7	8.3	13.3	25.3	6.6	19.5
CMAQ (BU)	14.1	5.7	8.8	5.0	1.5	2.1	8.3	3.6	6.5	18.5	6.6	9.1
CMAQ (TD)	16.0	6.3	8.6	3.7	1.3	2.8	9.3	3.9	6.6	19.9	6.8	8.9
CZS	N/A	N/A	N/A	5.1	5.1	10.9	N/A	N/A	N/A	20.4	11.8	10.9
CMAQ (BU)				11.6	4.9	7.1				23.1	9.1	11.3
CMAQ (TD)				10.7	5.0	7.3				23.1	9.1	11.3
SZS	17.8	10.2	14.7	7.9	8.0	14.9	14.2	9.0	13.1	23.2	12.5	15.1
CMAQ (BU)	14.5	6.0	7.1	13.3	5.3	7.1	6.2	2.9	6.3	19.6	7.8	11.7
CMAQ (TD)	15.5	6.3	7.1	11.7	5.0	7.7	6.9	3.0	6.3	19.9	7.9	11.7
Mean	17.6	10.6	15.3	5.8	6.5	11.2	11.5	7.1	11.1	24.0	12.5	16.4
CMAQ (BU)	17.6	7.1	9.1	11.7	4.6	6.3	8.7	3.9	6.8	22.5	8.4	11.2
CMAQ (TD)	18.7	7.4	9.1	9.7	4.3	6.7	9.4	4.1	6.8	22.9	8.5	11.0



**Table 3. The changed percentages of ozone concentration based on the sensitivity analysis for April 2016.**

	No reduction	-30% VOCs emissions	-60% VOCs emissions
No reduction	-	-8.9% (Case 2)	-19.5% (Case 7)
-30% NO <sub>x</sub> emissions	14.2% (Case 1)	7.1% (Case 3)	-2.1% (Case 4)
-60% NO <sub>x</sub> emissions	23.7% (Case 6)	19.8% (Case 5)	14.5% (Case 8)



**Table 4. The changed percentages of  $\text{NO}_3^-$ ,  $\text{NH}_4^+$  and  $\text{SO}_4^{2-}$  concentrations based on the sensitivity analysis for January 2016.**

	$\text{NO}_3^-$	$\text{NH}_4^+$	$\text{SO}_4^{2-}$	SNA
-30% $\text{NO}_x$ emissions (Case 9)	-3.3%	-1.2%	3.8%	-1.0%
-30% $\text{NH}_3$ emissions (Case 10)	-16.3%	-14.5%	-0.6%	-11.7%
-30% $\text{SO}_2$ emissions (Case 11)	2.0%	0.2%	-2.4%	0.5%
-30% ( $\text{NO}_x+\text{NH}_3+\text{SO}_2$ ) emissions (Case 12)	-15.5%	-15.5%	-4.0%	-12.4%



Figure 1.

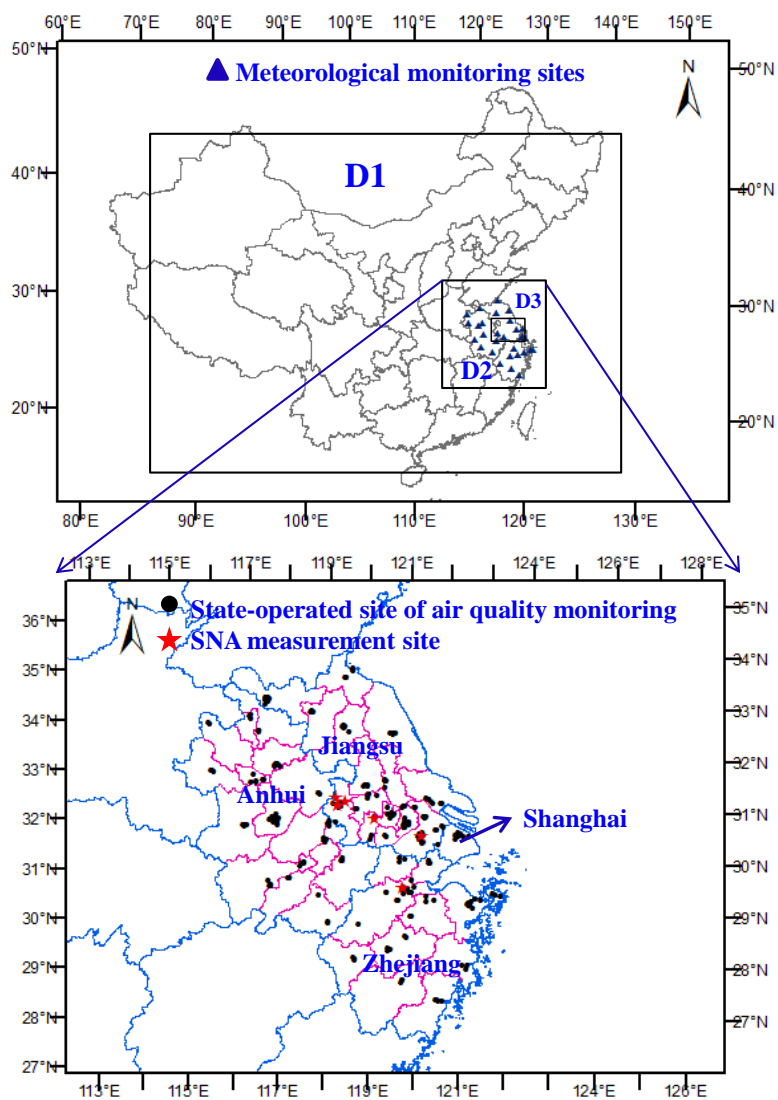




Figure 2.

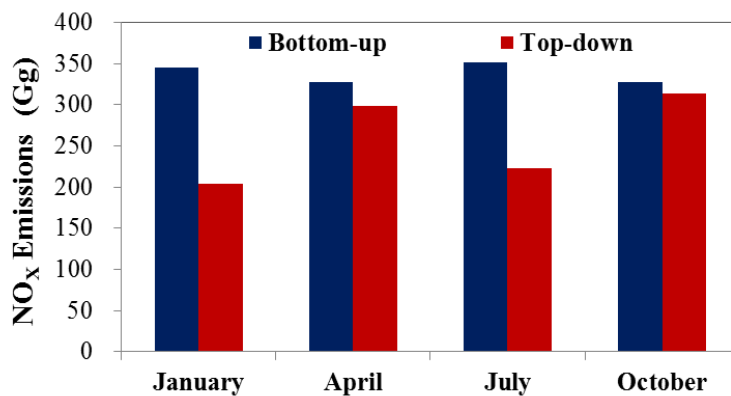




Figure 3.

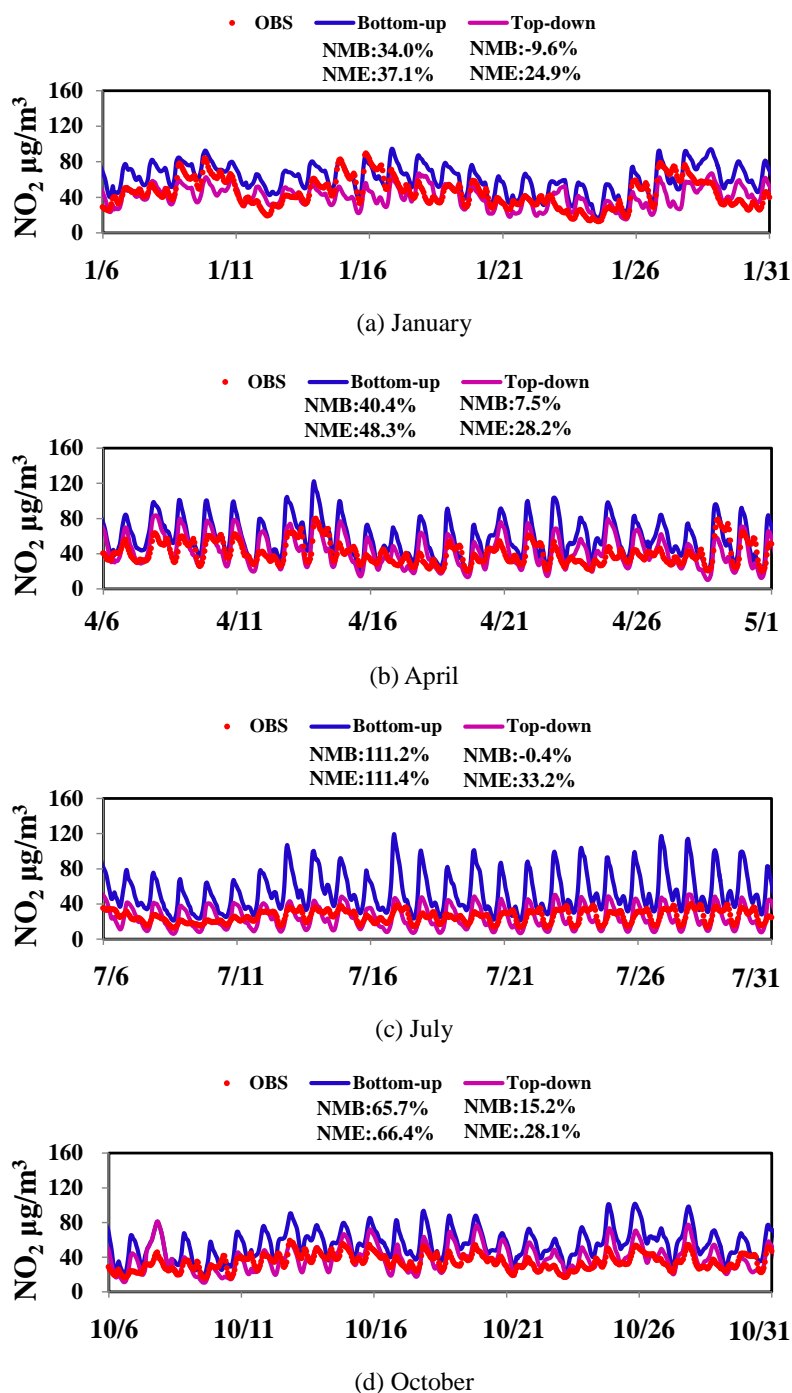




Figure 4.

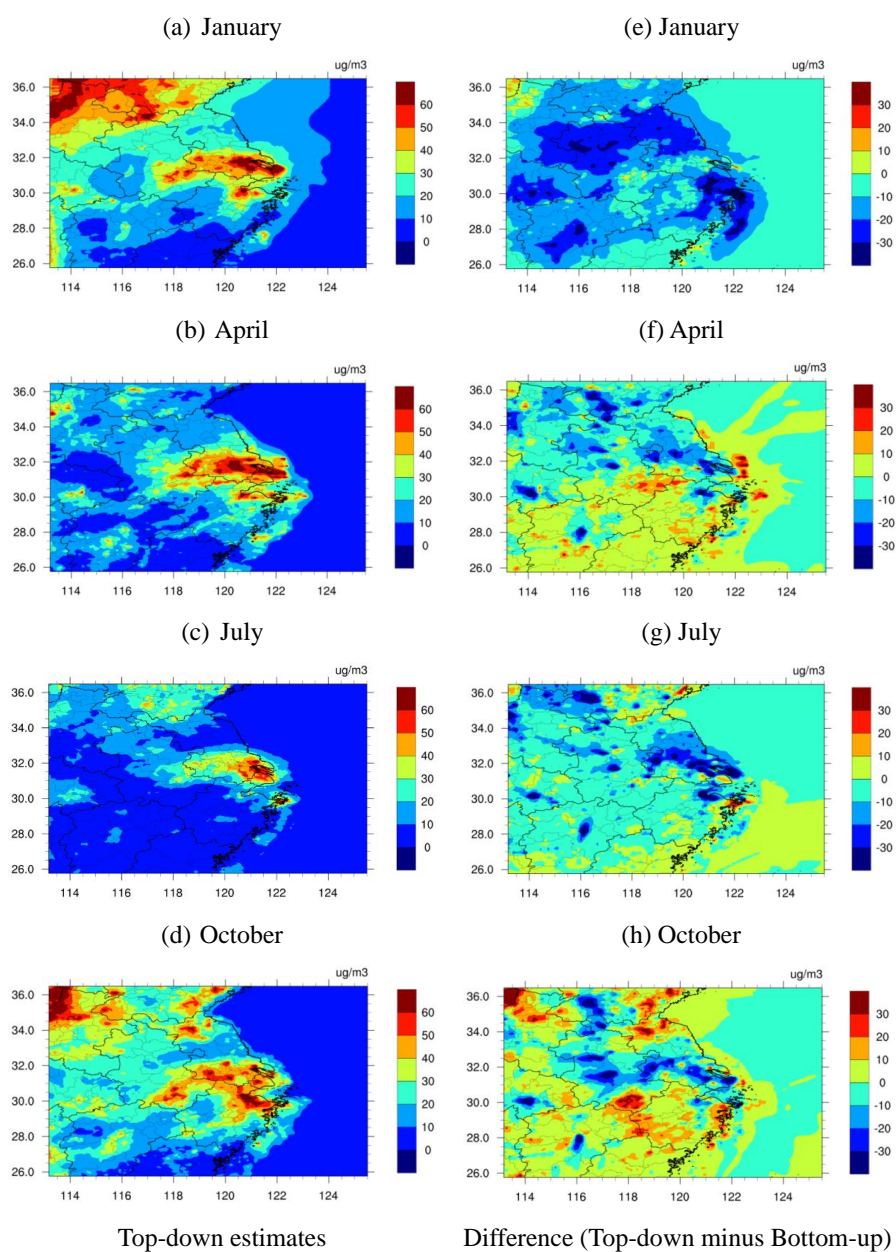




Figure 5.

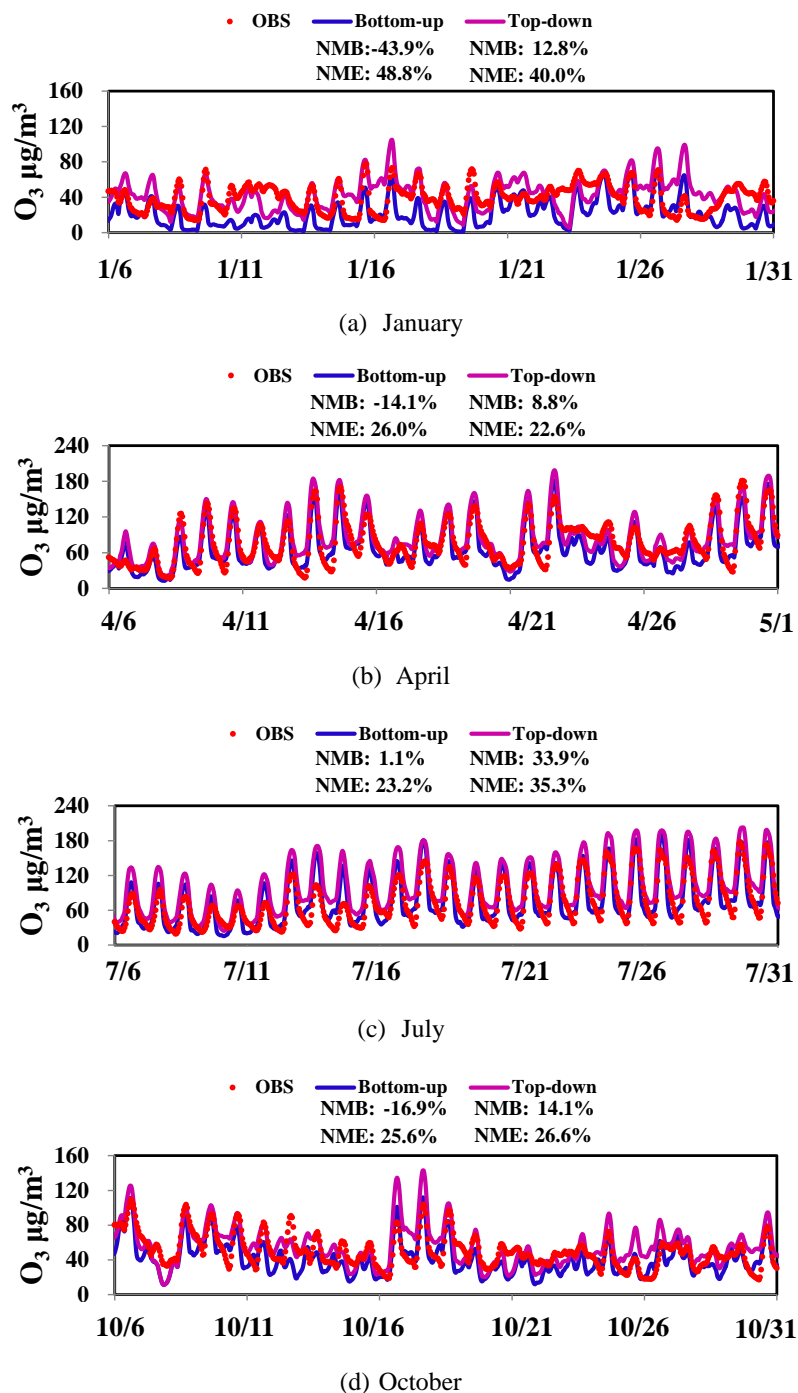




Figure 6.

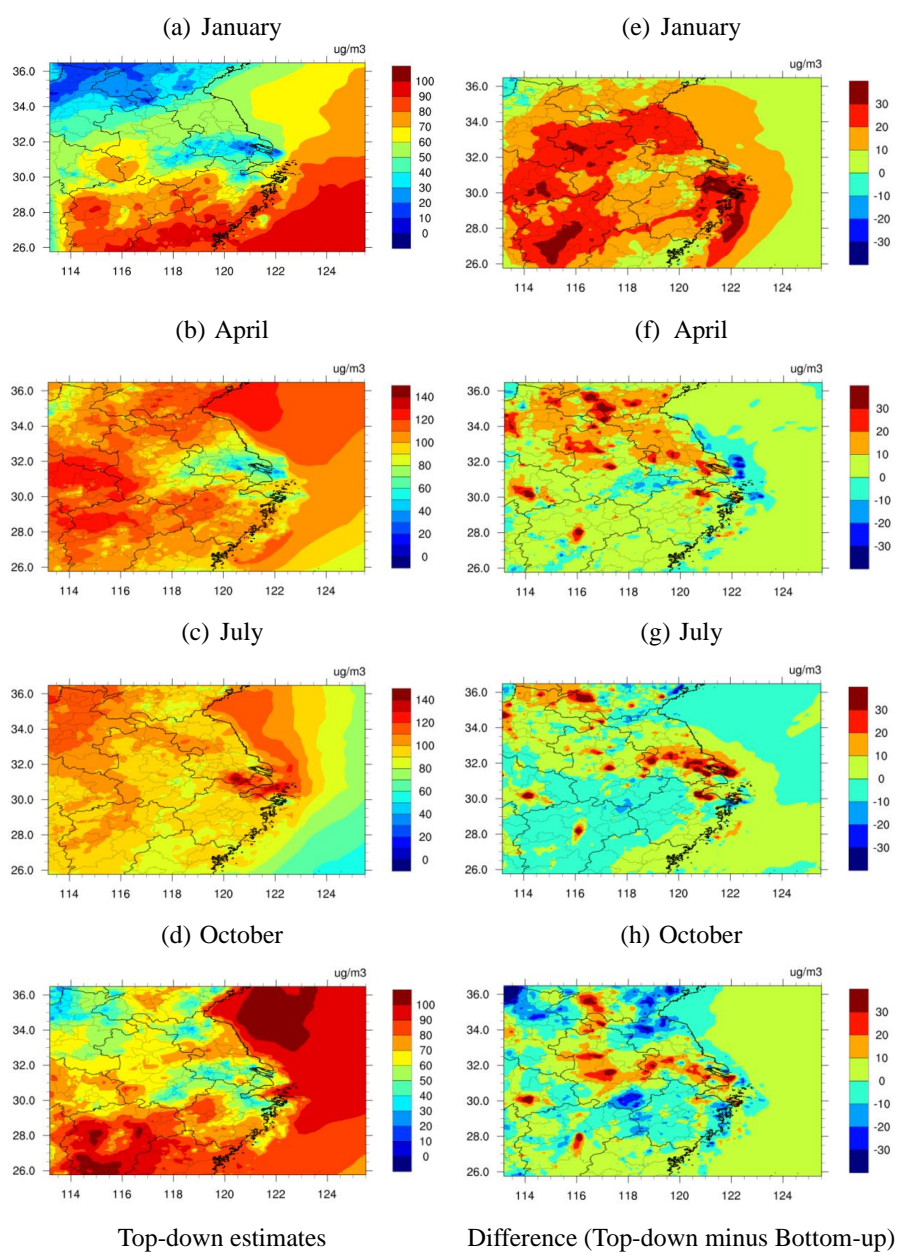




Figure 7.

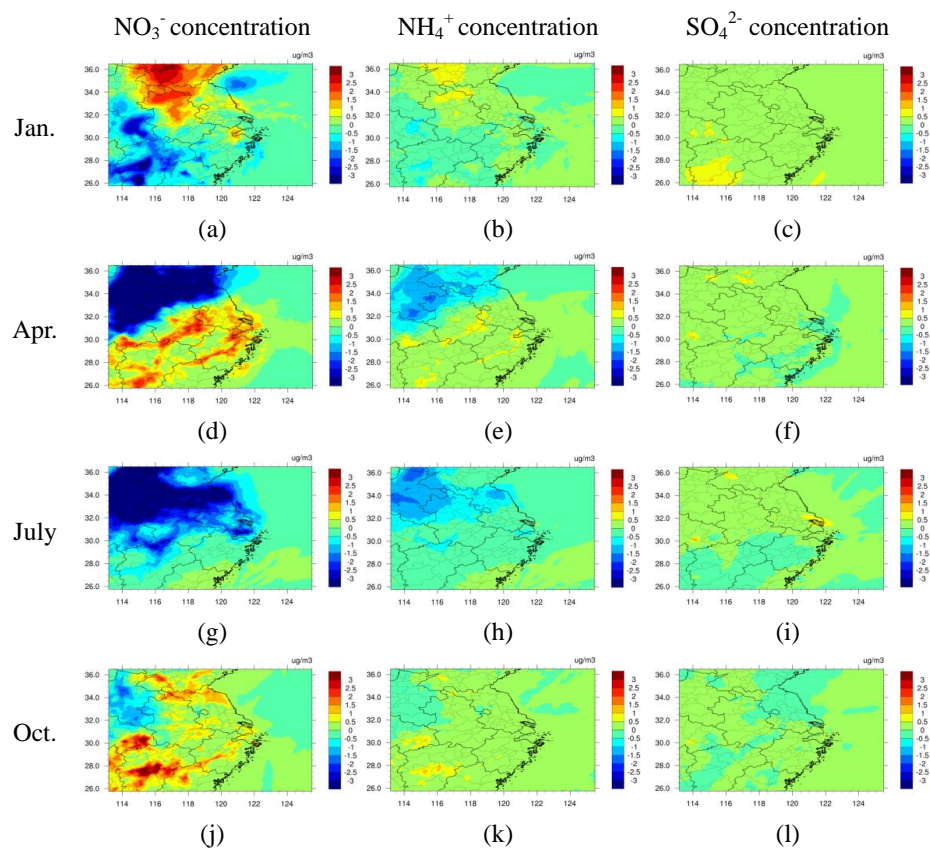




Figure 8.

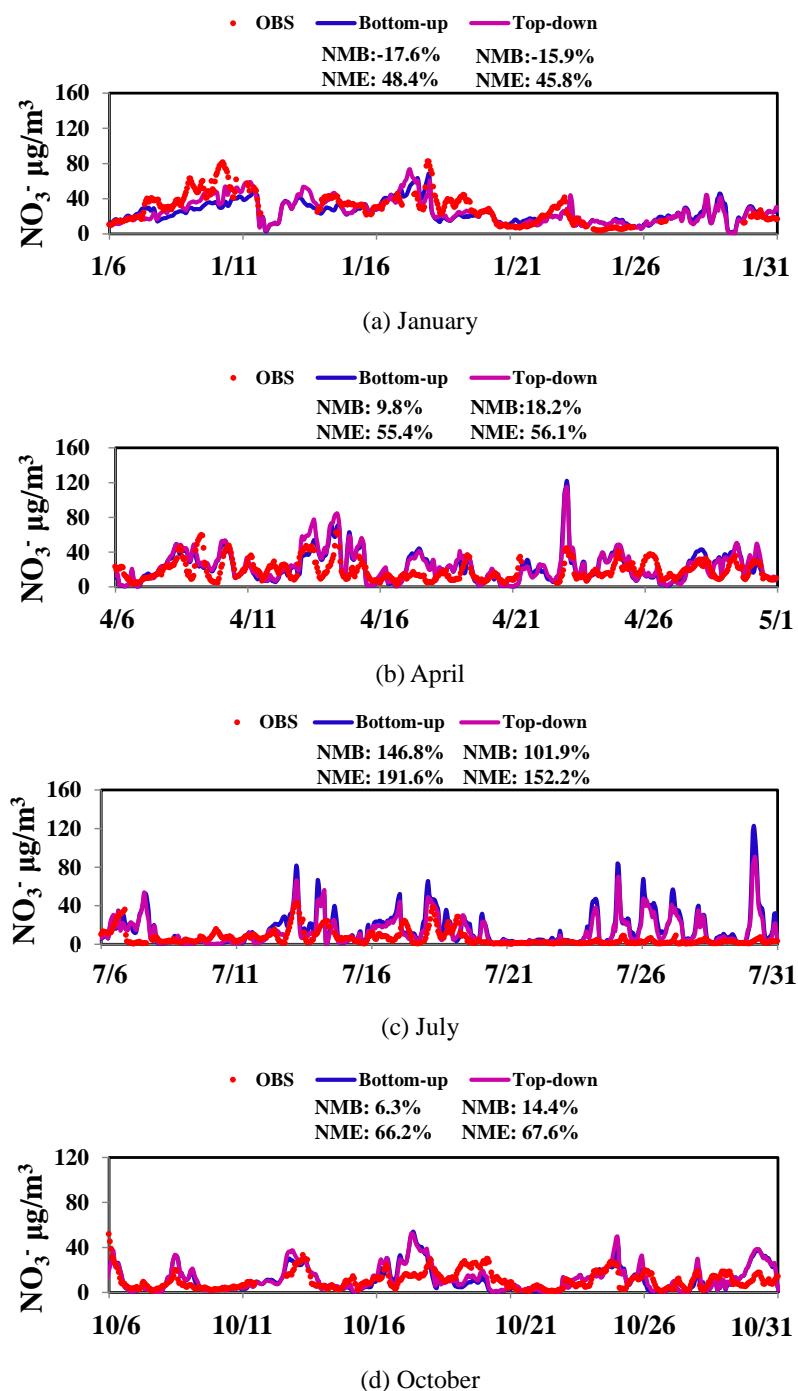




Figure 9.

